J. Fluid Mech. (2020), *vol.* 883, A45. © Cambridge University Press 2019
doi:10.1017/jfm.2019.911

Spatio-temporal dynamics of turbulent separation bubbles

Wen Wu[1,†], **Charles Meneveau**[1] **and Rajat Mittal**[1]

[1]Department of Mechanical Engineering, Johns Hopkins University, Baltimore, MD 21218, USA

(Received 26 May 2019; revised 20 August 2019; accepted 28 October 2019)

The spatio-temporal dynamics of separation bubbles induced to form in a fully developed turbulent boundary layer (with Reynolds number based on momentum thickness of the boundary layer of 490) over a flat plate is studied via direct numerical simulations. Two different separation bubbles are examined: one induced by a suction–blowing velocity profile on the top boundary and the other by a suction-only velocity profile. The latter condition allows reattachment to occur without an externally imposed favourable pressure gradient and leads to a separation bubble more representative of those occurring over airfoils and in diffusers. The suction-only separation bubble exhibits a range of clearly distinguishable modes, including a high-frequency mode and a low-frequency 'breathing' mode that has been observed in some previous experiments. The high-frequency mode is well characterized by classical frequency scalings for a plane mixing layer and is associated with the formation and shedding of spanwise-oriented vortex rollers. The topology associated with the low-frequency motion is revealed by applying dynamic mode decomposition to the data from the simulations and is shown to be dominated by highly elongated structures in the streamwise direction. The possibility of Görtler instability induced by the streamwise curvature on the upstream end of the separation bubble as the underlying mechanism for these structures and the associated low frequency is explored.

Key words: boundary layer separation, turbulence simulation

1. Introduction

Flow separation is ubiquitous in external as well as internal flows: wings and fuselages at high angles of attack, flow past external objects, shock-wave/boundary layer interactions, diffusers, corners, inlets and junctions are just a few examples of this kind of flow. In most of these applications, the incoming boundary layer is turbulent and separates either because of an adverse pressure gradient (APG) or a geometric discontinuity (e.g. backward-facing step). The separated flow typically exhibits unsteadiness across a broad range of time scales (see Eaton & Johnston 1982; Cherry, Hillier & Latour 1984; Kiya & Sasaki 1985; Najjar & Balachandar 1998; Tenaud *et al.* 2016; among others). These unsteady modes can dominate the dynamics of the separation bubble and they have significant implications for the

† Email address for correspondence: w.wu@jhu.edu

performance of the flow device/system at hand. They also introduce difficulties for prediction, but might also offer opportunities for active and passive control of these flows.

For turbulent separation bubbles (TSBs), a low-frequency unsteadiness at a time scale significantly larger than the convective time scale corresponding to the bubble is often observed (Wu *et al.* 2005; Hudy & Naguib 2007; Nadge & Govardhan 2014; Mohammed-Taifour & Weiss 2016; Tenaud *et al.* 2016). The phenomenon has been described as a 'breathing' or 'shrinkage and enlargement' of the separation bubble, or a 'flapping' of the separated shear layer. Compared with the high-frequency unsteady mode that represents the vortex generation in the shear layer (and whose time scale is still much larger than the small turbulent eddies' time scales), the low-frequency one is less well understood. Besides its impact on engineering equipment, the low-frequency motion is also a major source of uncertainty in measurements with relatively short averaging times and can cause significant difficulties in the modelling of these flows. It should be pointed out that most authors have not directly observed a distinctive low-frequency behaviour of the separation bubble itself, but they only detected a low frequency in velocity or in wall pressure fluctuations and attributed this frequency to a slight flapping motion of the separated shear layer. In what follows, we will summarize the previous work on the unsteadiness of various separating flows with particular focus on the low-frequency mode. Some of the important questions will be outlined, and the objectives to be pursued in this paper will be presented.

1.1. *Unsteadiness of separating flows*

Large-scale unsteadiness is observed in a wide range of configurations that produce flow separation. For geometry-induced flow separation, for example, researchers have examined flow separation at the leading edge of a blunt flat plate (Cherry *et al.* 1984), at the sharp corner of a backward-facing step (Eaton & Johnston 1982) or a diffuser (Kaltenbach *et al.* 1999) and around a hump (Marquillie & Ehrenstein 2003) or bluff body (Najjar & Balachandar 1998). Here, we briefly summarize the previous investigations that have described the unsteadiness quantitatively and proposed some possible mechanisms.

Among others, Cherry *et al.* (1984) and Kiya & Sasaki (1985) conducted experiments on flow separation on a two-dimensional rectangular leading-edge geometry and observed low-frequency motions. Cherry *et al.* (1984) described a low-frequency process as a slow modulation of the vorticity shedding from the reattachment zone, wherein the flow goes through pseudo-periodic shedding of large-scale vortical structures followed by a large-scale but irregular shedding of vorticity, and a relatively quiescent phase with the absence of any large-scale shedding structures. The relaxation time scale between shedding phases is approximately six times the primary vortex-shedding period. The cause of this low-frequency process was not explained. Kiya & Sasaki (1985) observed a low-frequency process at a similar time scale. Their observations, however, described the low-frequency kinematics as the slight lifting of the shear layer in the vertical direction (less than 4 % of the shear layer thickness) at a low frequency, which leads to a change in the vortices that are shed from the separation bubble. The passage and decay of the varying discrete vortices generate multiple crossings of the zero velocity in the reattachment region and with a short-time averaging it appears as a shrinkage and enlargement of the separation bubble. Following Eaton & Johnston (1982), they proposed that the origin of the low-frequency unsteadiness may be the change of

the spanwise coherence of the vortices and the variation in their ability to entrain momentum. Some high-fidelity simulations of similar configurations also show the presence of the low-frequency process whose cause was not elucidated (Tafti & Vanka 1991; Tenaud *et al.* 2016).

Another widely used configuration for the study of flow separation is the backward-facing step. Eaton & Johnston (1982) were the first to describe the low-frequency unsteadiness in this flow and they proposed several possible mechanisms for the low-frequency motions. Durst & Tropea (1982) and Nadge & Govardhan (2014), among others, support one proposed mechanism, namely of an instantaneous imbalance between shear layer 'entrainment from the recirculating zone' and 'reinjection of fluid near reattachment'. Heenan & Morrison (1998) employed a permeable plate in their experiments and suggested that the low frequency was due to a feeding back of the disturbances from the impingement point to the separation point. Some others attributed the low-frequency motion to the cutting off of the recirculation region from the separation bubble by a large structure which reaches the wall well upstream of the mean reattachment point (McGuineess 1978; Troutt, Scheelke & Norman 1984; Driver, Seegmiller & Marvin 1987; Hasan 1992). Other mechanisms that have been proposed include the growth and breakdown of the secondary recirculation region near the lower step corner (Spazzini *et al.* 2001; Hall, Behnia & Morrison 2003), and the absolute unstable mode of the recirculation region (Wee *et al.* 2004; Hudy & Naguib 2007). It is clear from this short and by no means exhaustive review that not only is a commonly accepted physical explanation for the low-frequency motion unknown presently, but evidence about whether a specific observed behaviour is a cause or a consequence of the unsteadiness is still lacking.

There are also numerous studies on the unsteadiness in the wake of bluff bodies that have implications for this research. Owing to the complex vortex shedding in the wake, the unsteadiness and occurrence of the low-frequency motion is usually explained by the imperfect synchronization and interaction between different types of vortical structures present in the flow (see Gerich & Eckelmann 1982; Najjar & Balachandar 1998; Wu *et al.* 2005; among others). In general, a geometry-induced flow separation is configuration-dependent and the mechanisms of the unsteadiness may vary from one configuration to another.

Flow separation can also be induced by an APG without the presence of a surface divergence. Compared with the geometry-induced fixed-point separation, a pressure-induced separation is not influenced by the surface curvature, thus being less configuration-dependent. Many investigations on flow separation fall in the category of APG-induced separation. Before reviewing previous research on pressure-induced separation, we will briefly summarize flow separation over airfoils, which is caused by a combination of a mild surface curvature and an APG. Because airfoils are streamline-shaped, the change in geometry is relatively moderate and the separation point is usually not at a fixed position, e.g. a sharp leading edge or step corner.

The study on flow separation over airfoils originates back to the observations of Jones (1934) and mainly focuses on laminar incoming flow. One critical feature of laminar flow separation over airfoils is an abrupt increase in the bubble length that occurs occasionally. Owen & Klanfer (1953) classified the closed separation region into 'short' and 'long' bubbles. The former were found where the length of the bubble is of the order of 1 % of the chord length and $O(10\delta_s^*)$ to $O(1000\delta_s^*)$, and 'long' bubbles with length of the order $O(10\,000\delta_s^*)$ (with δ_s^* being the displacement thickness at the point of separation). The 'bursting' from short to long bubbles crucially impacts the aerodynamic performance of the airfoil because a short bubble

only affects the pressure distribution locally while a long bubble can alter the overall pressure distribution around an airfoil (Tani 1964). Parameters such as local Reynolds number or pressure gradient in the region of the bubble (Gaster 1963), as well as semi-empirical models (Horton 1968), have been proposed to characterize the bubble bursting. While most studies have found that the bursting into a long bubble is caused by a small change in the incidence or speed, more recent investigation indicates the possibilities of an absolute instability that causes the bursting (Alam & Sandham 2000; Jones, Sandberg & Sandham 2008), or an acoustic feedback mechanism (Jones, Sandberg & Sandham 2010), or a coupling of viscous–inviscid interaction and free-stream disturbances (Marxen & Rist 2010). It is still an open question as to whether bubble bursting is driven by a change in the stability characteristics of the bubble or by some global instability of the flow. The low-frequency 'flapping' motion in the aft part of the separated shear layer is also reported in some studies on laminar separation bubbles (LSBs) over airfoils, but the reason is unknown (Hain, Kähler & Radespiel 2009).

To examine flow separation in the absence of surface curvature, experiments have employed the use of aspirated boundaries or contoured ceilings (either concave diverging–converging (Perry & Fairlie 1975; Patrick 1987; Weiss, Mohammed-Taifour & Schwaab 2015; Mohammed-Taifour & Weiss 2016) or convex converging–diverging (Marxen, Rist & Sagner 2003; Michelis, Yarusevych & Kotsnois 2018) configurations). Simulations have employed a variety of suction–blowing type boundary conditions on the top boundary of the computational domain (Na & Moin 1998*a*; Alam & Sandham 2000; Spalart & Strelets 2000; Kotapati *et al.* 2010; Marxen & Henningson 2010; Abe 2017; Seo *et al.* 2018; Wu & Piomelli 2018). For LSBs, it has been reported that the disturbance amplification agrees well with linear stability theory, often with an instability of the convective Kelvin–Helmholtz (KH) type. This is followed by a sudden breakdown to three-dimensional small-scale turbulence (Spalart & Strelets 2000; Rist & Maucher 2002; Marxen & Henningson 2010). Unsteadiness of the flow is mainly characterized by the shedding of spanwise rollers. Pauley, Moin & Reynolds (1990) were the first to attempt to simulate two-dimensional LSBs (Re_θ from 162 to 325). They found that some bursting reported in early studies (see Gaster 1963; among others) is actually periodic shedding that has been time-averaged. Spalart & Strelets (2000) reported a slight flapping of the separated shear layer in their study of LSBs at $Re_\theta = 180$ but claimed that the three-dimensionality sets in rapidly, thereby not allowing time for the development of other longer-time-scale unsteady motions.

Recently, Weiss *et al.* (2015) and Mohammed-Taifour & Weiss (2016) investigated the unsteady behaviour of a massively separated TSB generated by a combination of APG and favourable pressure gradient (FPG) ($Re_\theta = 5000$). In addition to broadband fluctuations associated with turbulence, the flow displayed a low-frequency 'breathing' or 'flapping' mode and a high-frequency 'shedding' mode (Weiss *et al.* 2015; Mohammed-Taifour & Weiss 2016). The frequencies of the two modes are centred at Strouhal number $St = fL_{sep}/U_\infty$ of 0.01 and 0.35 (L_{sep} is the length of the mean separation bubble), respectively. The shedding mode, as in the geometry-induced separations, can be characterized quite well by the KH instability of the separated shear layer. The origin of the low-frequency mode, however, is less clear. Weiss *et al.* (2015) and Mohammed-Taifour & Weiss (2016) mentioned that the counter-rotating vortices near the sidewalls of the tunnel may affect the unsteadiness. The frequency ranges they reported are close to that in the literature. Hudy & Naguib (2007) compared the frequencies observed in different experiments on geometry-induced separation and showed that they are nearly constant: $St \approx 0.08$–0.2 for the flapping

motion and 0.5–1.0 for the shedding motion. It is, however, unclear as to why the breathing mode appears to have a frequency that is approximately 10 times lower than that in fixed-separation flows.

Simulations provide the capability to examine the spatio-temporal dynamics of these TSBs in a way that is difficult to accomplish in experiments. The first direct numerical simulations (DNS) of a TSB were performed by Na & Moin (1998*a*) with $Re_\theta = 300$ and they observed that both the separation and reattachment were highly unsteady. However, these simulations did not exhibit any low-frequency motion and neither have any of the subsequent ones at $Re_\theta = 300$, 600 and 900 (Abe 2017), at $Re_\theta = 500$–1500 (Coleman, Rumsey & Spalart 2018) and at $Re_\theta = 2500$ (Wu & Piomelli 2018).

In order to address this gap, we conduct DNS of two types of separation bubble induced on a turbulent boundary layer developing on a flat plate. The first is a separation bubble similar to these previous studies, where separation is induced by applying a suction–blowing velocity on the top boundary of the computational domain. The second bubble is induced by a velocity profile that has suction only.

Flow separation is also a topic that has been studied extensively in the high-speed flow community. Two shock-induced separation configurations that have been extensively used in research are the compression ramp and the reflection of an incident shock wave impinging on the boundary layer. Low-frequency unsteadiness in both settings appears as a large-scale motion of the shock. There remain some outstanding questions and debates about the source and mechanism of the low-frequency motion in shock-induced separations (Dussauge, Dupont & Debiève 2006; Touber & Sandham 2009; Clemens & Narayanaswamy 2014). It has been shown that the source of the shock oscillations could be from either the upstream condition or the unsteady recirculating zone. There are, however, fundamental differences between the current TSB and shock-induced separation, including the presence of wave-propagation-associated feedback within the separated flow region and forced reattachment due to downstream shocks in the latter, and the relative shortness of shock-induced bubbles (approximately $(40$–$100)\theta_o$ compared to $(100$–$10\,000)\theta_o$ for pressure-gradient-induced TSBs).

1.2. *Motivations and objectives*

The vast majority of computational studies and many experimental studies of APG-induced separation have employed a suction-and-blowing configuration (Perry & Fairlie 1975; Patrick 1987; Na & Moin 1998*a*; Weiss *et al.* 2015; Abe 2017; Wu & Piomelli 2018; Wu *et al.* 2018). An advantage of this configuration is that the total mass flux at the inflow and outflow planes remains the same, and this might simplify the experiments as well as the analysis. However, this type of configuration generates an APG followed by an FPG and the latter leads to a forced reattachment of the flow. However, natural separating flows such as on airfoils and in diffusers do not have this type of forced FPG-driven reattachment, and we expect that this would also impact any low-frequency modes (breathing/flapping) that involve the opening and closing of the bubble. Motivated by these expectations, we initially compare a suction–blowing (or APG–FPG) induced separation bubble with a suction-only (APG only) induced separation bubble at the same Reynolds number. Subsequently, our attention focuses exclusively on the latter configuration, since it is more representative of separation flows in most applications, and we conduct a detailed analysis of the unsteadiness and spatio-temporal structure of this 'natural' TSB.

The suction-only pressure distribution has been used in previous experiments (Dianat & Castro 1991; Alving & Fernholz 1996; Song, DeGraaff & Eaton 2000;

Cases	$Re_{\theta,o}$	$Re_{\tau,o}$	$Re_{\delta,o}$	$[L_x \times L_y \times L_z]/\theta_o$	$N_x \times N_y \times N_z$	Δx_o^+	$\Delta y_{o,min}^+$	Δz_o^+
TSB-SB	490	200	4150	$935 \times 100 \times 117$	$2304 \times 408 \times 384$	9.6	0.58	7.2
TSB-SO	490	200	4150	$1170 \times 100 \times 117$	$3072 \times 408 \times 384$	9.0	0.58	7.2

TABLE 1. Simulation parameters: N_i is the number of grid points in the entire domain.

Dandois, Garnier & Sagaut 2007) and simulations (Pauley *et al.* 1990; Alam & Sandham 2000; Spalart & Strelets 2000), many of which have focused on LSBs (Pauley *et al.* 1990; Alam & Sandham 2000; Spalart & Strelets 2000). The mean features of the separation bubble have been extensively reported, but less attention has been given to the dynamics of suction-only separation bubbles or the low-frequency 'breathing' or 'flapping' behaviour. The present study on TSBs focuses on the low-frequency behaviour and provides detailed comparisons between the dynamics of suction–blowing and suction-only separation bubbles.

In the present DNS of natural TSBs, a massive, long separation bubble is induced, and the reattachment of the mean flow is due to the turbulent diffusion of momentum. Special attention is given to the unsteadiness of the separated flow. In particular, we examine the different time scales of the unsteadiness near the separation and reattachment point both in the vicinity of the wall and in the separated shear layer. We discuss the mechanisms that determine the unsteadiness by relating them to certain types of flow instability.

In the following, we first present details of the numerical methodology, and then discuss the mean field features, as well as the instantaneous flow evolution. We then describe the unsteadiness of the separation bubble and discuss possible underlying mechanisms. Finally, we draw the main conclusions and make recommendations for future work.

2. Methodology

2.1. *Configuration*

We perform DNS of a turbulent boundary layer (TBL) at $Re_\theta = U_o\theta_o/\nu = 490$, induced to separate via an APG generated by suitable application of a velocity boundary condition on the top of the computational domain. This Reynolds number is comparable to recent DNS of separating TBLs (e.g. Coleman *et al.* (2018) at $Re_\theta = 500$–1500 in the zero-pressure-gradient (ZPG) region, and Abe (2017) at $Re_\theta = 300$, 600 and 900). The Reynolds number is limited by the resolution demands imposed by the very long separation bubble that develops in this flow and the particularly long simulation time required to characterize the low-frequency motion. The subscript $(\cdot)_o$ refers to scales used for non-dimensionalization, namely the free-stream streamwise velocity and the momentum thickness at a streamwise location upstream of the APG region. The corresponding $Re_\tau = u_{\tau,o}\delta_o/\nu$, where δ_o is the boundary layer thickness at the reference plane, is $Re_\tau = 200$. The domain size, grid points and resolution used are listed in table 1 and the computational domain is shown in figure 1.

2.2. *Turbulent boundary layer upstream of the TSB*

The recycling and rescaling method by Lund, Wu & Squires (1998) is utilized to generate the inflow TBL. We also employ a constant spanwise shift of $L_z/2$ for the

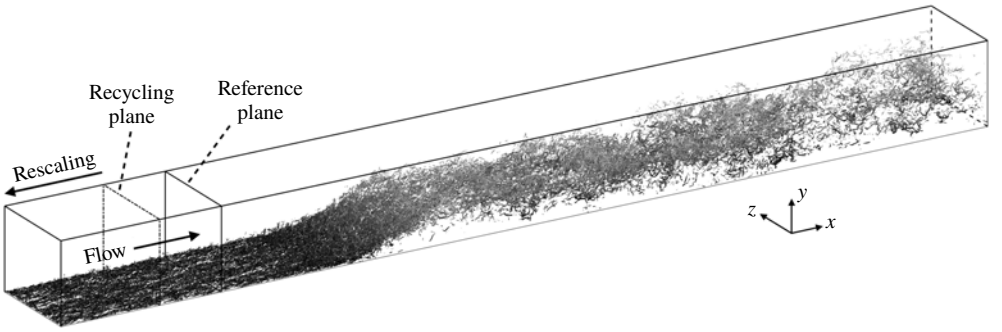

FIGURE 1. Computational domain. An instantaneous flow field of the TSB-SO case is shown in the domain, visualized by the isosurfaces of the second invariant of the velocity-gradient tensor $Q = -\frac{1}{2}(\partial u_j/\partial x_i)(\partial u_i/\partial x_j) = 0.0165U_o^2/\theta_o^2$. Note that x, y and z are, respectively, the streamwise, spanwise and wall-normal directions.

fluctuating components at each time step to reduce the streamwise correlation of the turbulence between the inlet and the recycling plane (Spalart, Strelets & Travin 2006). In the current configuration, the distance between the inflow and the recycling plane is greater than $17\delta_{rcy}$, or $125\theta_o$, larger than the minimum $11\delta_{rcy}$ recovery length suggested by Morgan *et al.* (2011) to avoid spurious periodicity. We use a large spanwise domain to prevent an artificial constraint to the turbulent structures in the separated shear layer (Abe *et al.* 2012; Asada & Kawai 2018). A doubling of the domain size in the spanwise direction shows negligible changes in the first- and second-order statistics of the flow (figure 3). We have also verified from shorter spatio-temporal maps (not shown) that the key features of the unsteadiness of the separation bubble, including the low frequency, also remain unchanged.

2.3. *Boundary conditions*

A convective boundary condition is used at the outflow and periodic conditions are employed at the spanwise boundaries. At the top boundary, a non-zero vertical velocity is prescribed so as to generate an APG in the domain, while the streamwise velocity satisfies zero vorticity and the spanwise velocity component has zero vertical gradient. Two different vertical velocity profiles are used in this study. The first is a suction–blowing (SB) type of profile, which is similar to the profile used in Abe (2017) and others, and is given by

$$V_{top} = V_{max}\sqrt{2}\left(\frac{x_c - x}{\sigma}\right)\exp\left[\psi - \left(\frac{x_c - x}{\sigma}\right)^2\right], \tag{2.1}$$

with $V_{max}/U_o = 0.3325$, $x_c/\theta_o = 10^6/2^{12} + 62.5$, $\sigma/\theta_o = 100\sqrt{2} \times 5^2/2^5$ and $\psi = 0.95$. This profile corresponds to a suction followed by blowing and leads to an APG followed by an FPG on the bottom wall, forming an inverted bell-shaped inviscid pressure profile on the lower wall (see figure 2). The net mass flux over the entire top boundary is zero. This case will be referred as 'TSB-SB' hereafter and used as a reference for comparison.

The other, suction-only (SO), profile is obtained by aiming to impose a pressure distribution over the bottom wall that has an APG profile that is similar to that over

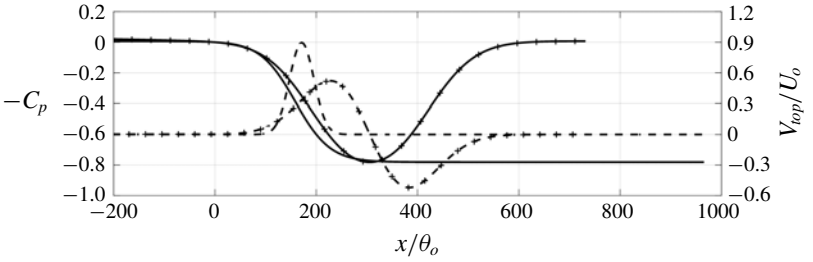

FIGURE 2. Profiles of the vertical velocity at the top boundary (– – –) and inviscid C_p at the bottom boundary (——). Lines with markers, TSB-SB; lines only, TSB-SO.

a typical airfoil section near stall. In particular, we use the pressure distribution of inviscid flow over the suction surface of a NACA 0012 airfoil at six degree angle of attack as a guide to obtain a suction velocity profile on the top surface. We employ a two-dimensional, inviscid solver for our rectangular computational domain and employ an iterative approach to adjust the free parameters (V'_{max}, x'_c and α) in the following velocity profile (see Pauley *et al.* 1990; Alam & Sandham 2000; Spalart & Strelets 2000)

$$V_{top} = V'_{max} \exp\left[-\left(\frac{x - x'_c}{\alpha L_y}\right)^2\right] \tag{2.2}$$

until we reach an APG profile that is a reasonable match to the target. The so obtained values of the profile parameters are $V'_{max}/U_o = 0.9$, $x'_c/\theta_o = 171.9$ and $\alpha = 0.3375$. The resulting profile and inviscid pressure coefficient $C_p = 2(P_w - P_{w,o})/U_o^2$ (where $(\cdot)_w$ denotes quantities at the wall) are also shown in figure 2. With this suction velocity applied at the top boundary, the nominal deceleration (Pauley *et al.* 1990)

$$S = \frac{1}{L_y U_o} \int V_{top}(x)\, \mathrm{d}x \tag{2.3}$$

is 0.54. This is much higher than the range that has been presented in previous studies on LSBs, i.e. 0.09 to 0.3 (Pauley *et al.* 1990; Spalart & Strelets 2000). The value is in line with the fact that a TBL is harder to separate than a laminar one due to the turbulence-enhanced momentum transfer. Downstream of $x = 300\theta_o$ we have ZPG and allow the separation bubble to develop naturally without any imposed pressure gradient. This suction-only case will be referred as 'TSB-SO' hereafter. Note that the start of these two velocity profiles imposed at the top boundary is far downstream of the recycling plane to ensure that the TBL at the recycling plane is not affected by suction.

In the current simulation, we employed a very long domain (the domain length is $935\theta_o$, although most figures do not show the entire domain) in the streamwise direction, and particular attention has been paid to ensure that large-scale structures have decayed significantly near the outflow. It should be noted that, in this incompressible flow simulation, there is no mechanism for propagation of spurious reflections from the outflow boundary (Don & Gottlieb 1990). Usually in an incompressible flow simulation, spurious reflected waves accumulate at the exit and lead to numerical instability; this does not happen in the current simulations due to the large domain chosen. Finally, the flow-through time of a fluid particle between

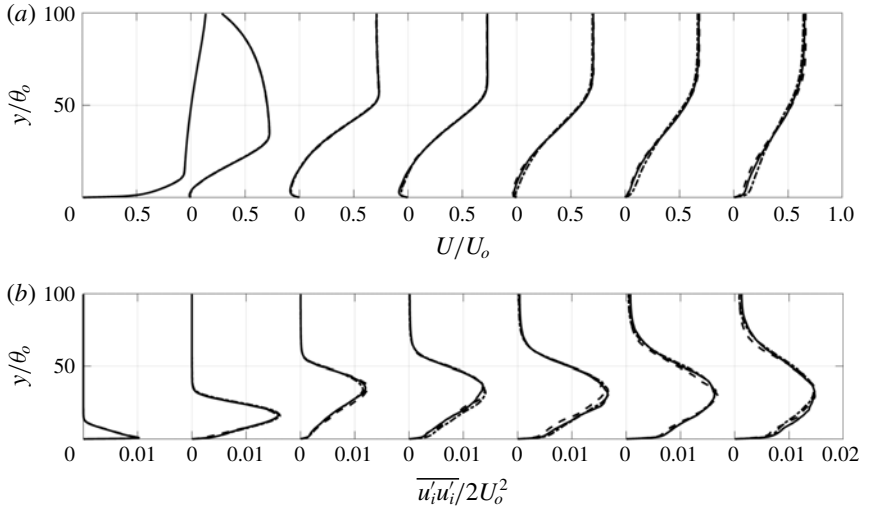

FIGURE 3. Profiles of mean (*a*) streamwise velocity and (*b*) turbulent kinetic energy of the TSB-SO case. Solid line, coarse grid; dashed line, fine grid; dash-dotted line, coarse grid with spanwise domain size doubled. The examining locations are $x/\theta_o = 100, 200, \ldots, 700$ (showing from left to right). Each profile is shifted to the right by 1 unit in (*a*) and 0.02 units in (*b*) for clarity.

the inflow and outflow is approximately $1500\theta_o/U_o$ (note that the mean streamwise velocity is approximately $0.6U_o$ after the suction extracts 54 % of the incoming fluid) and this is substantially larger than the time scale associated with the low-frequency motion, further indicating that the low-frequency mode is not associated with the domain size.

2.4. *Numerics*

The calculations are carried out using a well-established flow solver that solves the incompressible Navier–Stokes equations on a Cartesian cell-centred, collocated (non-staggered) grid (Mittal *et al.* 2008; Wu *et al.* 2018). The spatial derivatives are computed using a second-order-accurate, central-difference scheme. A second-order Adams–Bashforth scheme is employed for the convective terms and the diffusion terms in the horizontal directions. The diffusion term in the vertical direction is discretized using an implicit Crank–Nicolson scheme that eliminates the viscous stability constraint. The equations are integrated in time using a two-stage fractional step method. The Poisson equation for the pressure is solved by a pseudo-spectral method wherein the three-dimensional Poisson equation is transformed into a set of one-dimensional equations in the wall-normal direction using a Fourier transform in the periodic spanwise direction and a cosine transform in the streamwise direction. Each one-dimensional Helmholtz equation is then solved with the Thomas algorithm for each wavenumber set (k_x, k_z) before transforming back into the physical space coordinates. The method is second-order-accurate in time and space.

The grid resolutions are listed in table 1. A uniform grid is employed in the streamwise and spanwise directions, and a stretched grid in the wall-normal direction near the bottom wall with a maximum stretching rate of 1.6 %. The grid is also clustered in the wall-normal direction near the upper boundary. For the near-wall

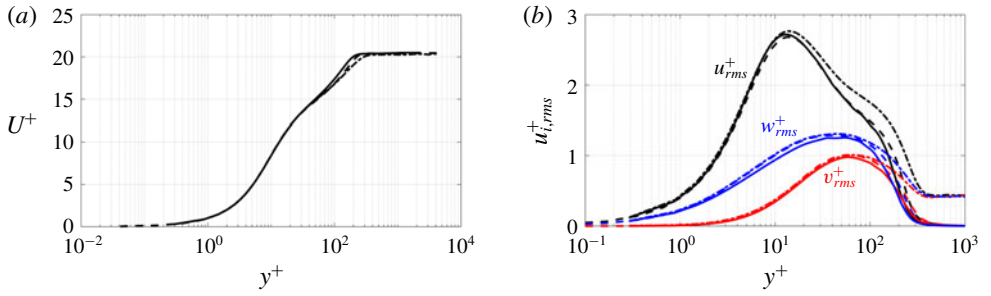

FIGURE 4. Comparison of (*a*) mean velocity and (*b*) Reynolds normal stresses in wall units at $Re_\theta = 670$ for validation: ——, current results; – – –, Schlatter & Örlü (2010); and — · —, Wu *et al.* (2017).

	$\Delta x/\delta^*_o$	$\Delta y_{max}/\delta^*_o$	$\Delta z/\delta^*_o$
Present	0.24	0.25	0.19
Spalart & Coleman (1997)	0.57	0.27	0.21
Na & Moin (1998*a*)	0.85	0.41	0.48
Skote & Hanningson (2002)	0.65	0.30	0.21
Abe (2017)	0.32	0.26	0.13

TABLE 2. Comparison of grid resolution between present simulation (case TSB-SO) and previous DNS of TSB.

flow, the grid size in wall units (wall units are obtained using the local friction velocity u_τ) are comparable to the values used in other DNS studies on separating TBLs (refer to table 2). Compared with the Kolmogorov scale η, the present resolution gives $\Delta x/\eta \leqslant 1.3$, $\Delta z/\eta \leqslant 1.1$ and $\Delta h/\eta \leqslant 2$ (where $\Delta h = \sqrt{\Delta x^2 + \Delta y^2 + \Delta z^2}$). Since the maximum dissipation of turbulence occurs at a length scale of approximately 24η (Pope 2000), the present grid is able to resolve a substantial part of the dissipation spectrum.

For the TSB-SO case, a grid that is 20 % finer in each direction (i.e. Δh is halved) over the entire calculation domain shows minor differences in the mean velocity and Reynolds stresses, showing that the calculation is grid-converged (figure 3). The code has been validated by performing an initial simulation of a ZPG TBL at $Re_\theta = 670$ and comparing the results with previous DNS by Schlatter & Örlü (2010) and Wu *et al.* (2017). The mean velocity and velocity fluctuations are shown in figure 4 and the agreement is very good.

The data are sampled at a regular time interval of $\Delta t = 3.89\theta_o/U_o$, once a statistically stationary state was reached. To characterize the unsteadiness at low frequency, the simulation is integrated over a very long duration of $T = 20\,000\,\theta_o/U_o$ and statistics are obtained by averaging over time and in the spanwise direction. The difference between the first- and second-order statistics obtained using only half of the sample and the ones using the entire data series is less than 1 %. In the following discussion, the averaged quantities will be denoted via capital letters for primary flow variables, and by $\overline{(\cdot)}$ for turbulent statistics. Quantities that are only averaged in the spanwise direction are denoted by $\langle\cdot\rangle_z$, and other arbitrary averaging by $\langle\cdot\rangle$.

Cases	x_{sep}/θ_o	x_{ratt}/θ_o	L_{sep}/θ_o	h_{sep}/θ_o
TSB-SB	188	379	191	18.5
TSB-SO	164	614	450	16.4

TABLE 3. Characteristics of the mean separation bubble. The mean separation point x_{sep} is where $C_f = 2\tau_w/U_o^2 = 0$ and $\mathrm{d}C_f/\mathrm{d}x < 0$; the mean reattachment point x_{ratt} is where $C_f = 0$ and $\mathrm{d}C_f/\mathrm{d}x > 0$; and h_{sep} is the maximum distance between the contour line of $U = 0$ and the wall.

3. Results and discussion

3.1. *Suction–blowing (SB) versus suction-only (SO) separation bubble*

In this section, we compare the key features of these two separation bubbles. This is followed by a detailed analysis of the unsteadiness in the TSB-SO bubble.

3.1.1. *Vortex topology*

Figure 5 shows instantaneous snapshots of the vortex structures in the two separation bubbles via the second invariant of the velocity-gradient tensor

$$Q = -\frac{1}{2}\frac{\partial u_j}{\partial x_i}\frac{\partial u_i}{\partial x_j} = \frac{1}{2}(\Omega_{ij}\Omega_{ij} - S_{ij}S_{ij}), \tag{3.1}$$

where Ω_{ij} and S_{ij} are the antisymmetric and symmetric parts of the velocity-gradient tensor, respectively. It can be seen that many elongated low-speed regions are present in the separated shear layer. The size of these structures in the spanwise direction is relatively small near the separation point and they merge into larger structures as the flow separated. Each of them is surrounded by a group of streamwise-aligned hairpin-like structures. In the TSB-SB case these structures are broken by the blowing, and near-wall streaks form during its recovery to TBL after reattachment. In the TSB-SO cases the structures in the separated shear layer sustain for a long time and break around $x = 450\theta_o$ at the time instant shown. A large vorticity packet is observed downstream, including small-scale turbulent eddies nested inside the packet.

3.1.2. *Characteristics of the mean flow*

Figure 6 shows contours of mean streamwise velocity U/U_o in the x–y plane together with several selected mean streamlines for both the separation bubbles. The characteristic properties of the mean separation bubble are also compared in table 3. The mean separation bubble in the TSB-SO configuration is significantly longer than that in the TSB-SB case but slightly thinner. Furthermore, the reversed flow in the TSB-SO configuration has a lower magnitude, and the streamwise velocity gradient near the reattachment point is also lower due to the absence of the forced impingement of the flow. The peak reversed flow amplitude, scaled with the far-field velocity at each streamwise location, is approximately 8 % in TSB-SO and 11 % in TSB-SB.

The time-mean profiles of skin-friction coefficient (C_f) and pressure coefficient on the wall (C_p) for both the bubbles are compared in figure 7. In both cases the wall pressure agrees well with that for an inviscid solution up to the separation point. The suction-and-blowing configuration produces a bell-shaped inviscid wall pressure profile over the surface that consists of an APG followed by an FPG (Na & Moin 1998*a*;

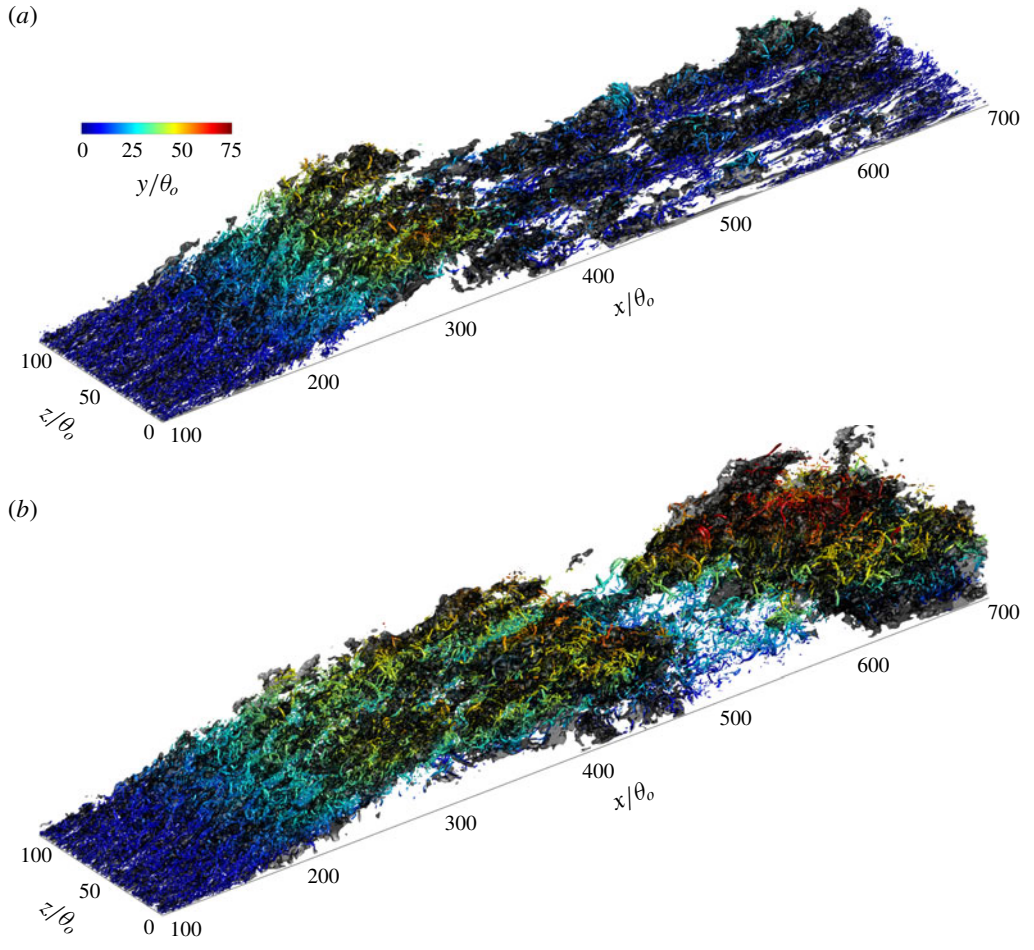

FIGURE 5. Vortex structures at one time instant for two separation bubbles: (*a*) TSB-SB and (*b*) TSB-SO. Vortex structures are visualized by the isosurfaces of the second invariant of the velocity-gradient tensor $Q = 0.0165U_o^2/\theta_o^2$ (see text), coloured by the distance from the wall. The dark-grey isosurfaces are $u' = -0.1U_o$.

Abe 2017; Wu & Piomelli 2018). Pressure profiles of realistic separated flow are, however, quite different. For an airfoil at large angle of attack, a steep APG appears near the leading edge of the airfoil and gradually decreases towards the trailing edge. However, there is usually no region of FPG (Rinoie & Takemura 2004; Kim *et al.* 2009; Asada & Kawai 2018). In diffusers with fixed opening angle in the streamwise direction (Kaltenbach *et al.* 1999), strong APG occurs at the beginning of the deflected wall and decreases rapidly to ZPG downstream. Unless the wall itself is not parallel to the free-stream flow (e.g. a shock-induced separated flow at a compression corner), there is no common mechanism to have a driving mean flow that impinges towards the surface after the flow separates.

The C_p in the TSB-SO configuration consists only of the APG as expected, and there is no local pressure peak due to the stagnation of the mean flow such as the one observed at $x/\theta_o \sim 390$ in the TSB-SB case. In both cases, the Clauser

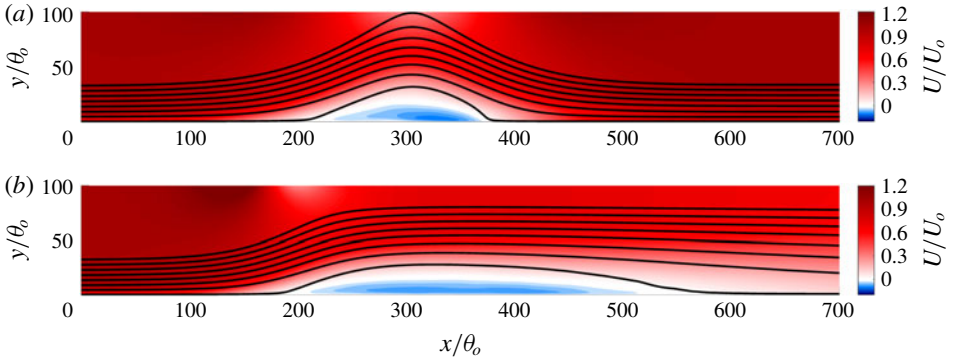

FIGURE 6. Contours of mean streamwise velocity with selected streamlines (solid): (*a*) TSB-SB and (*b*) TSB-SO.

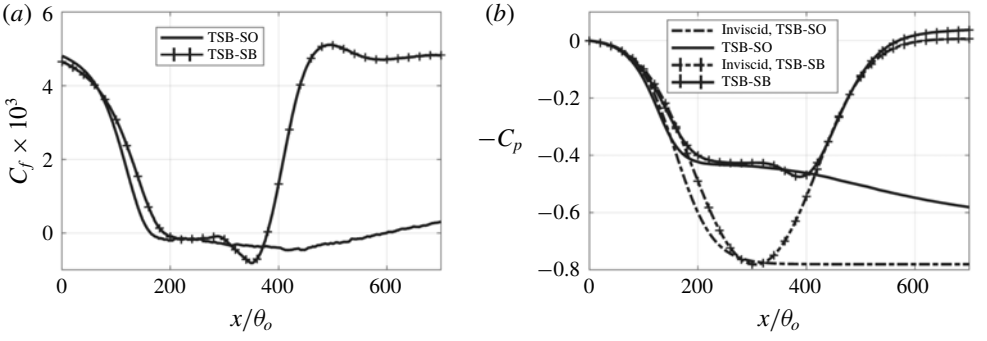

FIGURE 7. Streamwise profiles of C_f and C_p. Lines with markers, TSB-SB; lines only, TSB-SO; dash-dotted lines in right panel, inviscid wall C_p.

pressure-gradient parameter

$$\beta = \frac{\delta^*}{\tau_w}\frac{\mathrm{d}P_e}{\mathrm{d}x}, \tag{3.2}$$

where $(\cdot)_e$ denotes the quantity measured at the edge of the boundary layer, is $\beta = 0.5$ at $x = 60\theta_o$, $\beta = 3$ at $x = 100\theta_o$, and then rapidly increases to $\beta = 85$ before u_τ becomes smaller than $0.01U_e$ upstream of the separation bubble.

The probability distribution of reverse flow occurring in the x–y plane is shown in figure 8 for both bubbles. The point of the separation region in both cases shows a very steep gradient in probability, indicating a stationary separation point. However, the reattachment behaviour of the two bubble is quite different. In particular, unlike the TSB-SB bubble, for the TSB-SO bubble there is a large region beyond the reattachment point where reverse flow can occur up to 10 % of the time. This is because the reattachment of the mean flow in the case of the TSB-SO bubble is due to the transport of momentum by turbulence and not forced due to the imposed blowing at the top. In order to confirm this statement, we examine the balance of momentum flux (Abe 2019) in the aft portion (i.e. the region between the bubble crest and the reattachment point) of both separation bubbles (figure 9). In the TSB-SB case, the convection term dominates the positive gain in the momentum balance near

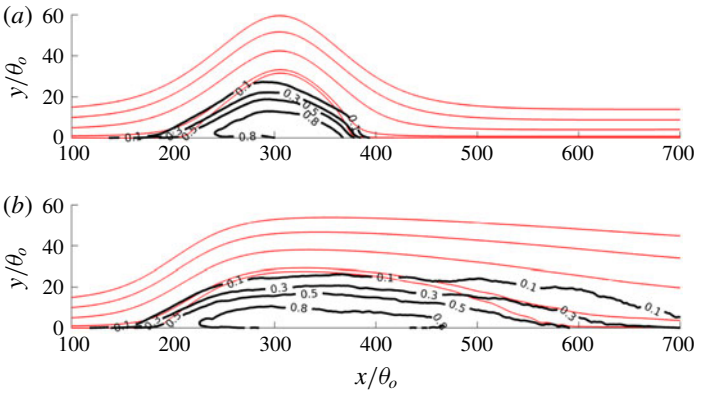

FIGURE 8. Probability of occurrence of reversed flow as a function of position: (*a*) TSB-SB; (*b*) TSB-SO. Light solid lines are selected mean streamlines.

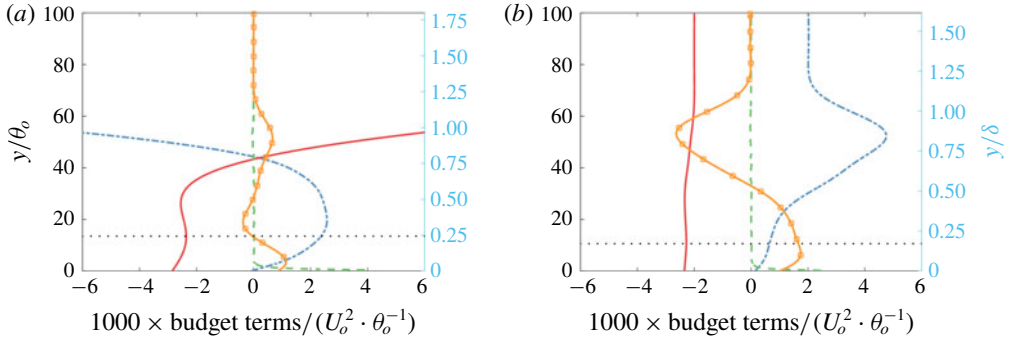

FIGURE 9. Budget of the mean x-momentum balance. Dash-dotted line, advective term $-U_j \partial U/\partial x_j$; solid line, pressure term $-\partial P/\partial x$; dashed line, viscous term $\nu \partial^2 \overline{U}/\partial x_j^2$; solid line with marker, Reynolds stress term $-\partial \overline{u'u'_j}/\partial x_j$; horizontal dotted line, local $y|_{U=0}$. (*a*) TSB-SB at $x/\theta_o = 342$. (*b*) TSB-SO at $x/\theta_o = 467$. The examining x-location is chosen as the middle point between the bubble crest and the mean reattachment point. The residual in both cases is smaller than $2 \times 10^{-4}\, U_o^2/\theta_o$.

the $U = 0$ 'interface', with a small turbulent transport term. In the TSB-SO case, on the contrary, the turbulent transport becomes the leading term in TSB-SO at such interface, and the mean flow only contributes near the edge of the boundary layer. On the wall, the region between $x/\theta_o = 600$ and $x/\theta_o = 706$ experiences backflow during 50 % to 30 % of the time for the TSB-SO bubble. The extent of this region in the TSB-SB case, in comparison, is only approximately $6\theta_o$ ($x/\theta_o \in [379, 385]$). The periodic formation of a discrete vorticity packet causes remarkable intermittency in flow reattachment: for 30 % (10 %) of time the bubble is 20 % (40 %) longer than the mean. As will be described later in the paper, this feature of the reattachment is associated with a low-frequency 'breathing' or 'flapping' of the TSB-SO bubble.

Eliminating the forced impingement due to the imposed blowing also significantly impacts the development of turbulence in the two flows as shown in figure 10. While the two cases share a similar turbulence profile near the region of initial separation, the TSB-SO case also exhibits another large area of high turbulence down near and

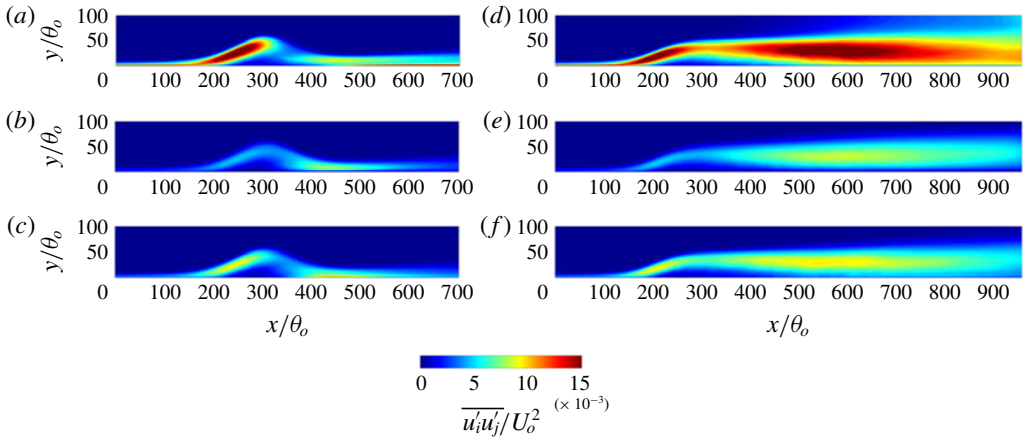

FIGURE 10. Time- and spanwise-averaged Reynolds normal stresses: (*a–c*) TSB-SB; (*d–f*) TSB-SO; (*a,d*) $\overline{u'u'}/U_o^2$; (*b,e*) $\overline{v'v'}/U_o^2$; and (*c,f*) $\overline{w'w'}/U_o^2$.

above the mean reattachment point. As will be shown later in the paper, this large region of turbulent fluctuations is associated with unsteady motions that occur at a large time and spatial scale. In general, the observed Reynolds stress distributions obtained for the TSB-SO case are in much better qualitative agreement with the ones in flow separation over an airfoil (Jones *et al.* 2008; Balakumar 2017) than those for the TSB-SB case. More details about the statistics of the TSB-SB bubble may be found in Wu, Meneveau & Mittal (2019).

3.1.3. *Low-frequency unsteadiness in the separation bubbles*

In this section, we examine the two separation bubbles for the presence of a low-frequency 'breathing' or 'flapping' mode. In figure 11 we show contours of instantaneous streamwise velocity and the velocity vectors in the x–y plane at centre span at two different time instants. The TSB-SO bubble shows large variation of shape in time: the bubble is long, enclosing a continuous backflow region (figure 11*c*) at some times, and has several distinct backflow regions at other times (figure 11*d*). The TSB-SB bubble, on the other hand, does not show any such large-scale changes in the size of the bubble with time (figure 11*a,b*). This behaviour also explains the differences in the probability distributions observed in figure 8 in the rear part of the TSB-SO bubble.

The change in the size of the separation bubble versus time serves as a simple parameter that measures large-scale unsteadiness of a separation bubble. The history of the total reversed flow area in the x–y plane, i.e. $A_{r,xy} = \int_{\Omega_r} \mathrm{d}x\,\mathrm{d}y$, where Ω_r is the region where $\langle u \rangle_z < 0$, is plotted in figure 12. A large-amplitude, low-frequency variation of the total backflow area is clearly observed for the TSB-SO bubble, whereas a similar behaviour is missing the TSB-SB bubble. Thus, taken together, figures 11 and 12 clearly suggest that, while the TSB-SO bubble exhibits a large-scale low-frequency unsteadiness of the type that has been characterized as the 'breathing' or 'flapping' mode in previous studies, the TSB-SB bubble does not show any such distinct behaviour.

Note that the low-frequency motion we observed here does not have a very significant separation in time scale with respect to the high-frequency ones. As we

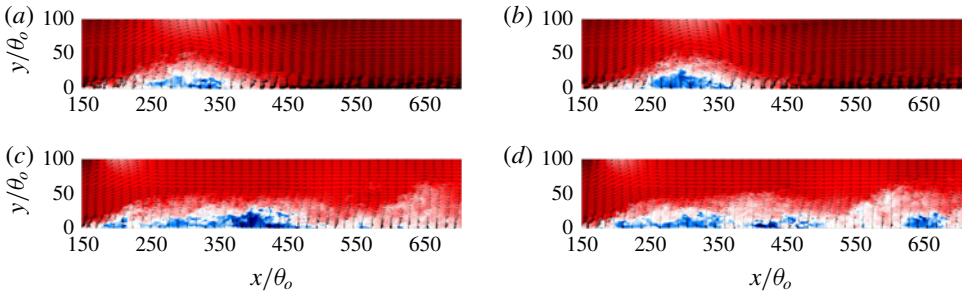

FIGURE 11. Instantaneous streamwise velocity and velocity vector in the x–y plane at $z = L_z/2$: (*a*) TSB-SB, $tU_o/\theta_o \approx 9260$; (*b*) TSB-SB, $tU_o/\theta_o \approx 11\,170$; (*c*) TSB-SO, $tU_o/\theta_o \approx 15\,000$; and (*d*) TSB-SO, $tU_o/\theta_o \approx 16\,950$. For colour maps, refer to figure 6.

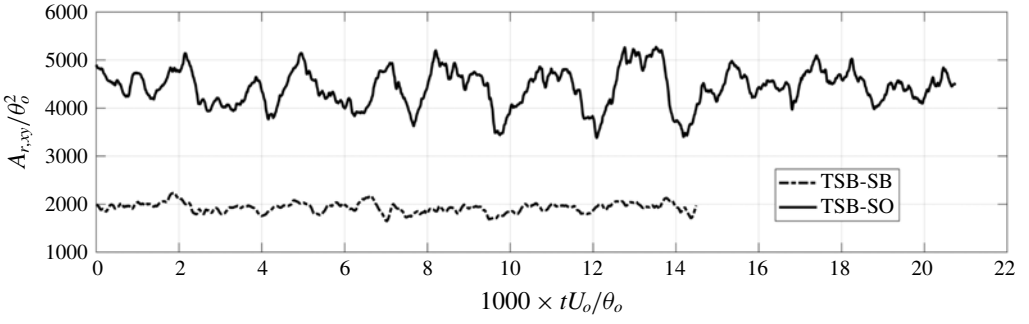

FIGURE 12. Time history of the total reversed flow area in the x–y plane.

will describe in detail in the next section, the frequencies of the two motions differ only by a factor of 2–2.5. As summarized in the Introduction, researchers have reported low-frequency motions that occur at a time scale ranging from 6 to 35 times longer than the vortex shedding mode. One reason for this discrepancy may be that we are observing a different type of low-frequency motion in flow separation. It also is possibly related to the relatively low Reynolds number of the current flow since it is expected that, while the vortex shedding frequency scales with the inverse of the boundary layer thickness (which decreases with increasing Reynolds numbers), the low-frequency mode scales with the size of the separation bubble, which would be less dependent on the Reynolds number. Indeed, in the experiments of TSBs conducted by Weiss *et al.* (2015) and Mohammed-Taifour & Weiss (2016), the boundary Reynolds number was $Re_\theta = 5000$ and they observed a low-frequency peak in the spectrum that was 35 times lower than the vortex shedding peak. Note that, in their experiments, which employed a ceiling with an expansion and mass removal followed by a contraction, there is an FPG following the APG but the net FPG is smaller than the net APG. Thus their configuration falls in between what we define as SB and SO configurations.

3.2. *Characteristics of unsteadiness in the TSBs*

We begin by examining more closely the reversed flow in the vicinity of the wall for the TSB-SO bubble. The spatio-temporal map of the spanwise-averaged streamwise

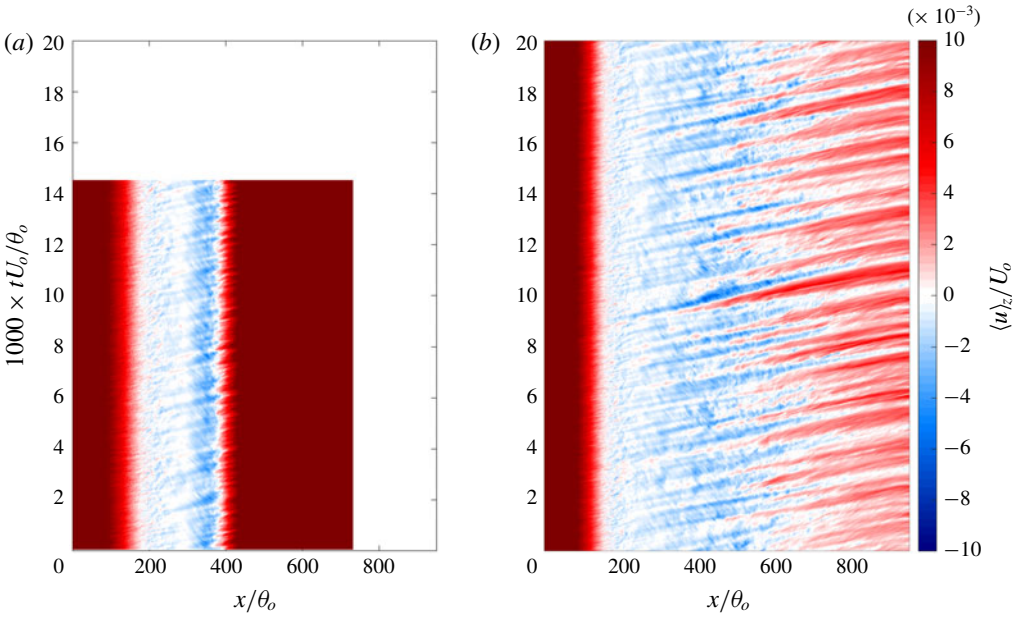

FIGURE 13. Spatio-temporal map of the spanwise-averaged streamwise velocity at the first grid point away from the bottom wall for: (*a*) TSB-SB bubble; (*b*) TSB-SO bubble. Some region in the left panel is left blank intentionally so that the two panels have the same axis range, because the TSB-SB case was integrated to $t = 14\,300\,\theta_o/U_o$ with a smaller domain in x.

velocity at the first grid point away from the wall is plotted in figure 13. For this separation bubble, besides the fluctuation of the incoming TBL at a very short time scale, a high-frequency unsteadiness is featured as parallel stripes separated in time by approximately $TU_o/\theta_o \approx O(400)$ in the map. Also, strong forward flow is observed to penetrate into the reversed flow region up to $x/\theta_o = 400$, and this occurs on a time scale that is larger than that at the upstream region of the separation bubble. The low-frequency motion does not appear in the TSB-SB case, in which the reversed flow stripes exhibit the same temporal interval near the separation and reattachment regions.

Note that the time scale shown here has no direct link to the ones described in figure 12: figure 13 represents the local (i.e. x) intermittency of the flow on the wall, describing the streamwise motion of a band-like, quasi-two-dimensional separated region. Figure 12, on the other hand, is an integral quantity over the entire x–y domain describing the total reversed flow area. When a discrete vorticity packet sheds off from the separating shear layer, for instance, it will show as unsteadiness in figure 13 but not in figure 12 until the discrete vorticity packet decays and the reversed flow diminishes.

Figure 14 plots the pre-multiplied power density spectra of the velocity shown in figure 13. The data series is windowed and detrended and the analysis uses a total of 11 equal-length segments in time with 50 % overlap (Na & Moin 1998*b*; Abe 2017). Each segment contains 896 samples (stored every 100 time steps). The resulting resolved frequency range is $0 \leqslant f\theta_o/U_o \leqslant 0.129$. On the upstream end of the separation bubble (i.e. $x/\theta_o \approx 200$), a clear peak appears at a frequency of approximately $f_h\theta_o/U_o \approx 0.0025$. At the other end of the separation bubble ($x/\theta_o > 400$)

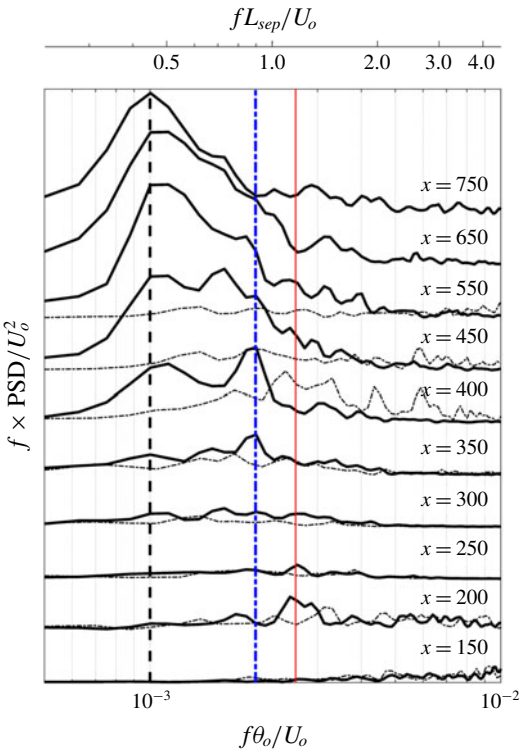

FIGURE 14. Pre-multiplied energy spectrum of the streamwise velocity shown in figure 13: dash-dotted, TSB-SB; solid, TSB-SO. Each plot is shifted upwards by 7×10^{-7} units for clarity. The thin red vertical solid line marks the high frequency $f_h = 0.0025U_o/\theta_o$; the dashed black vertical line represents the low frequency $f_l = 0.001U_o/\theta_o$; and the dash-dotted blue vertical line is $f_m = 0.002U_o/\theta_o$.

the spectrum is dominated by a low frequency corresponding to approximately $f_l\theta_o/U_o \approx 0.001$. The spectrum also indicates a peak corresponding to a frequency of $f_m\theta_o/U_o \approx 0.002$ in the region $(350–400)\theta_o$. We refer to this as the 'mid-frequency' but, as we will discuss later in the paper, this mode and the one at $f_l\theta_o/U_o \approx 0.0025$ seem to be driven by the same vortex rollup mechanism. Overall, the low and high frequencies show a clear separation in both scale ($f_h\theta_o/U_o \approx 0.0025$ versus 0.001) and location (high frequency for $x/\theta_o < 250$ and low frequency for $x/\theta_o > 250$), with the x/θ_o from 350 to 400 appearing as a region of transition between these two distinct regions of the flow. The low frequency coincides with the subharmonic of the medium-frequency motion, which indicates that the former could be a result of vortex pairing.

The unsteadiness exhibited in the spanwise-averaged field should not be interpreted as implying that the underlying mechanism is dominated by two-dimensional motions. Instead, it suggests that the spatial signature of the low-frequency motion is visible in the spanwise-averaged flow and this is indeed consistent with the notion of 'breathing' or expansion and contraction of the bubble. While figure 13 corresponds to the data extracted very near the wall, similar frequency peaks and scale separation are also observed within the separated shear layer. Figure 15(*a*) shows contours of the fluctuating pressure p'_{rms} and figure 15(*b–d*) shows the pre-multiplied energy

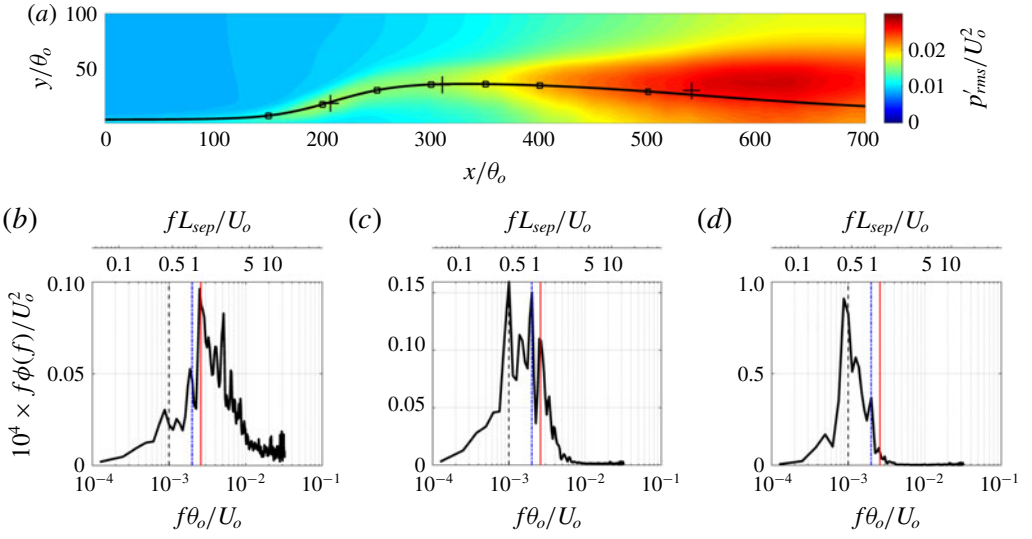

FIGURE 15. Pre-multiplied energy spectrum of the pressure fluctuation at several locations in the separated shear layer. (*a*) Contour map of p'_{rms}; the cross markers indicate the locations where the spectra are obtained (that is, $x/\theta_o = 207.3$ for (*b*), 310.3 for (*c*) and 540.0 for (*d*)). The square markers are the locations where the two-point correlation is evaluated; the solid line is the selected mean streamline passing the high-p'_{rms} regions. (*b–d*) Pressure spectra. The thin red solid vertical line marks the high-frequency $f_h = 0.0025U_o/\theta_o$; the black dashed vertical line represents the low frequency $f_l = 0.001U_o/\theta_o$; and the blue dash-dotted vertical line marks $f_m = 0.002U_o/\theta_o$.

spectrum of pressure fluctuations at several locations within the high-p'_{rms} regions. As for the velocity spectrum shown above, the pressure data series are windowed and detrended with 50 % overlap, and the spectra are averaged over all the grid points in the spanwise direction at each location. The peaks of the spectrum agree well with those for the reversed flow on the wall. One difference is that the low-frequency motion already appears at $x = 200\theta_o$ in the separated shear layer, while it shows up much further downstream on the wall. This indicates that this low-frequency mode originates from the separated shear layer and impacts the near-wall flow after its effects spread downstream. Note that the ellipticity of the pressure does not seem to be the cause for this because such low-frequency motion is not observed in figures 13 and 14 near the separation point.

The Strouhal number defined as $St_{L_{sep}} = fL_{sep}/U_o$ is 1.125, 0.9 and 0.45 for f_h, f_m and f_l, respectively, in the TSB-SO case. The high-frequency mode also appears in the TSB-SB case but the Strouhal number differs by a factor of 2.4 due to the different L_{sep}. In previous studies using the suction–blowing configuration (Na & Moin 1998*a*; Abe 2017), a motion at $St \approx 0.35$ has been reported as the 'shedding mode'. In our TSB-SB case, this value is close to 0.4, which agrees reasonably well with the literature. The fact that the same phenomenon (i.e. KH vortex shedding) in the two configurations gives different $St_{L_{sep}}$ indicates that L_{sep} is not the best parameter to characterize the unsteadiness of a separation bubble. In the current study we associate the motion at frequency f_l with the low-frequency motion even though its Strouhal number is higher than in some previous studies, because this motion agrees phenomenologically with the 'breathing' phenomenon associated with

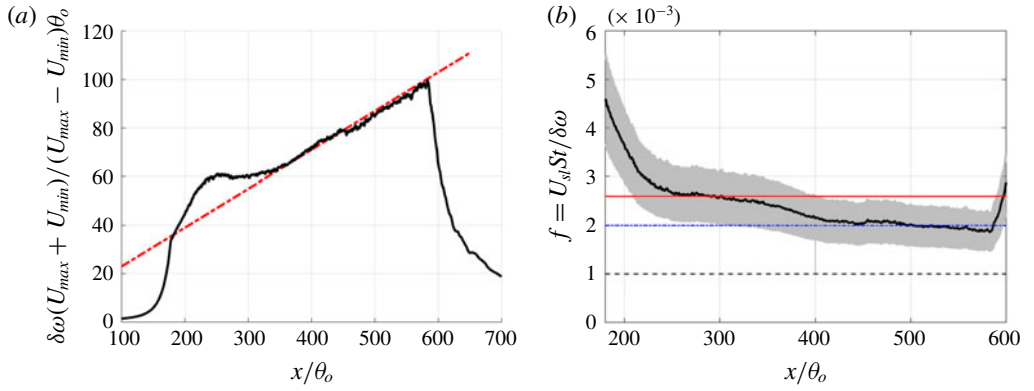

FIGURE 16. (*a*) Profile of the normalized vorticity thickness: ——, TSB-SO; — · —, $\mathrm{d}\delta_\omega/\mathrm{d}x = C_{\delta_\omega}(U_{max}-U_{min})/(U_{max}+U_{min})$, $C_{\delta_\omega}=0.16$. (*b*) Dominant frequency of mixing layer predicted by canonical mixing layer relationship: ——, $St_{\delta_\omega}=0.25$; grey hatched region, $St_{\delta_\omega}\in[0.2,\ 0.3]$. The thin solid horizontal line marks the high frequency $f_h = 0.0025U_o/\theta_o$; the dash-dotted horizontal line marks $f_m = 0.002U_o/\theta_o$; and the dashed horizontal line represents the low frequency $f_l = 0.001U_o/\theta_o$.

the low-frequency motion in earlier studies of incompressible separation bubbles (Pauley *et al.* 1990; Spalart & Strelets 2000; Weiss *et al.* 2015; Mohammed-Taifour & Weiss 2016).

Previous studies have shown that the separated shear layer is similar to a canonical plane turbulent mixing layer (e.g. velocity and Reynolds stress scale well by the mixing layer scaling) and the high-frequency motion may be generated by KH instability (e.g. large-scale spanwise structures) (Na & Moin 1998*a*; Spalart & Strelets 2000; Rist & Maucher 2002; Marxen & Henningson 2010; Abe *et al.* 2012; Abe 2017). To examine the degree of similarity to a mixing layer, we have examined the profile of the vorticity thickness δ_ω defined as

$$\delta_\omega = (U_{max}-U_{min})/(\partial U/\partial y)_{max}, \tag{3.3}$$

where U_{max} and U_{min} are the maximum and minimum time- and spanwise-averaged streamwise velocities in the two sides of the separated shear layer. We find that (see figure 16*a*) δ_ω exhibits a linear growth with x after an initial transition at the beginning of the separation. The growth rate also agrees very well with the one found in previous studies on plane mixing layers (Liepmann & Laufer 1947; Brown & Roshko 1974; Pantano & Sarkar 2002; Abe 2017).

It has been widely reported in previous studies that the dominant frequency in a turbulent mixing layer corresponds to a Strouhal number $St_{\delta_\omega}=f\delta_\omega/U_{sl}\approx 0.2$–$0.3$ (with $U_{sl}=(U_{max}+U_{min})/2$). Figure 16(*b*) plots the frequency predicted by this relationship in the current simulation where we have used the local δ_ω. It can be seen that with $St_{\delta_\omega}=0.25$ the scaling predicts a frequency $f\theta_o/U_o$ ranging from approximately 0.004 to 0.002 in the $200 < x/\theta_o < 250$ region, which is very much in line with the two observed high frequencies of $f_m\theta_o/U_o = 0.002$ and $f_h\theta_o/U_o = 0.0025$ in this region of the bubble. In particular, the profile shows one plateau upstream of $x/\theta_o = 350$ and another downstream. This agrees very well with the locations where the spectral peaks appear in figure 14. This provides strong support for the notion that the mechanism

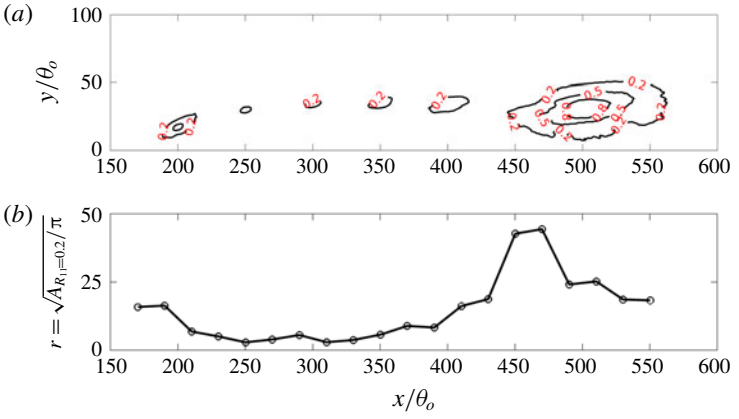

FIGURE 17. (*a*) Contours of two-point correlation coefficient of streamwise velocity fluctuations with levels of correlation indicated by text. The reference locations are selected along a mean streamline passing the high-p'_{rms} regions and are indicated by square markers in figure 15(*a*). The contours for different reference locations are superposed. (*b*) The nominal radius of the roller vortex determined from the area enclosed by the $R_{11} = 0.2$ contour line, i.e. $r/\theta_o = \sqrt{A/\pi}$.

of high- and medium-frequency unsteadiness is the KH instability of the mixing layer. Moreover, the plot shows that, despite a decrease in this predicted frequency with downstream distance, it never reaches the observed low frequency of $f_l\theta_o/U_o = 0.001$. This suggests that some mechanism other than KH instability drives the low-frequency unsteadiness in the rear part of the separation bubble.

Because the vortices generated by KH instability are spanwise rollers, we have examined the length scale of the flow in the separated shear layer, using the two-point autocorrelation coefficient in the x–y plane,

$$R_{11}(\boldsymbol{x}_{ref}, \boldsymbol{x}_{ref} + \Delta\boldsymbol{x}) = \frac{\langle u'(\boldsymbol{x}_{ref})u'(\boldsymbol{x}_{ref} + \Delta\boldsymbol{x})\rangle}{\langle u'(\boldsymbol{x}_{ref})u'(\boldsymbol{x}_{ref})\rangle}, \tag{3.4}$$

where $\Delta\boldsymbol{x}$ is the spatial separation between the reference location and the other locations in the computational domain. Several reference locations are chosen along a mean streamline passing through the high-p'_{rms} regions and the correlation is calculated between each of them and all the other locations in the flow fields. The contours of the correlation coefficients are shown in figure 17, where the R_{11} contour lines for selected reference location are presented on the same plot. If we define non-negligible correlation as $R_{11} \geqslant 0.2$, it can be seen (figure 17*b*) that the spanwise roller starts to generate near $x/\theta_o = 250$ and gradually grows in size. Between $x/\theta_o = 400$ and 500, the vortex length scale increases abruptly, suggesting the formation of large-scale vortex structures, possibly associated with the merging of the spanwise rollers.

Contours of the second invariant of the velocity-gradient tensor at one selected time (corresponding to the time instant shown in figure 5*b*) are shown in figure 18 and in the turbulent shear layer, the spanwise rollers consist of small-scale eddies. A large-scale conglomeration of vortices is formed near $x/\theta_o = 450$ at the time shown, and this seems to be in line with the notion that the large scales at this downstream location may be caused by a vortex merging process.

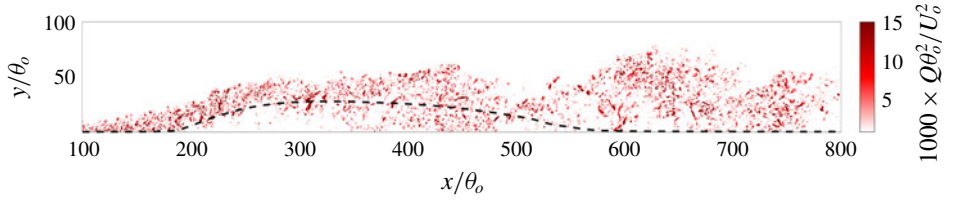

FIGURE 18. Contours of instantaneous secondary invariant of the velocity-gradient tensor in the x–y plane $z = L_z/2$ at $tU_o/\theta_o = 16\,950$. Only the positive Q are shown for clarity. The mean separating streamline is shown as the dashed line for reference.

It is, however, not clear whether this vortex merging is the mechanism underlying the low-frequency unsteadiness or whether the latter arises due to some other distinct mechanism. In particular, there are a number of possible candidate mechanisms for the low-frequency unsteadiness of the separation bubble, which include the following.

(*a*) Imbalance of entrainment from the recirculation region by the shear layer and the reinjection of fluid near the reattachment point (Eaton & Johnston 1982); this makes the separating shear layer flap towards the wall and significantly slows down its convection downstream.

(*b*) Shear layer switches from a convective instability to a global instability, which leads to local amplification. In laminar flows, researchers have found that global instability occurs when the mixing layer is formed by counter-streams and when $R_u = (U_{max} - U_{min})/(U_{max} + U_{min})$ exceeds 1.315 (Huerre & Monkewitz 1985; Strykowski & Niccum 1991), or the peak reversed flow amplitude exceeds 20 % of the free-stream velocity (Hammond & Redekopp 1998; Rist & Maucher 2002). In the current flow, the maximum value of R_u is 1.25 and the peak reversed flow magnitude is $0.08U_o$. Thus, this is not likely to be the mechanism.

(*c*) Some mechanism unrelated to the KH vortices, which breaks down the sheet of the spanwise vortices.

In general, it is not straightforward to separate cause from effect in a fully saturated, highly turbulent flow with a large range of temporal and spatial scales. In the current study, we employ dynamic mode decomposition (DMD) (Schmid 2010; Chen, Tu & Rowley 2012) to examine the flow field and to extract features/modes of the flow that correspond to the dominant time scales in the flows. The topology of these extracted modes is then used as the basis to further investigate the underlying mechanism for the low-frequency 'breathing' mode.

3.3. *DMD-based analysis of the three-dimensional flow field*

The basic idea of DMD analysis is to extract a low-dimensional description of a linear transformation that maps any snapshot of data from a dynamical system into the subsequent snapshot. The eigenvalue decomposition of this linear transformation then provides frequency information as well as the corresponding spatial structures. Furthermore, a projection of the snapshots onto these structures gives the amplitude (contribution) information (Schmid 2010; Sayadi *et al.* 2014). Eventually, the snapshots can be approximated using the DMD modes as

$$\Phi_r(\mathbf{x}, t) = \sum_{k=1}^{r} b_k \psi_k(\mathbf{x}) \exp(\omega_k t), \quad k = 1, 2, \ldots, r, \tag{3.5}$$

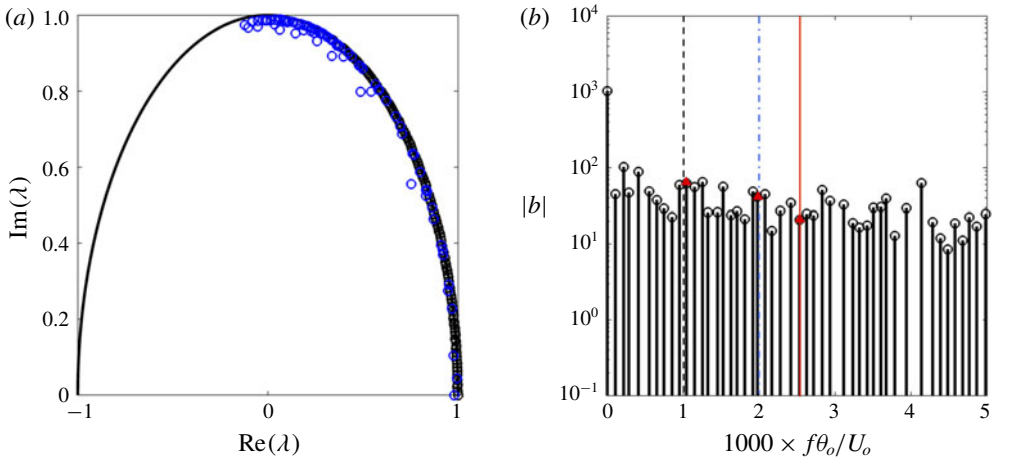

FIGURE 19. (*a*) Eigenvalues of the DMD modes. (*b*) Spectrum of the DMD modes; the range of the *x*-axis is limited to the frequency range of concern. Modes whose $|\lambda| < 0.995$ are shown by blue markers in (*a*) and are not included in (*b*). The three thin vertical lines refer to figure 15. The red triangular markers show the selected DMD modes closest to the three target frequencies.

in which Φ_r, ψ_k and b_k are the field reconstructed by the r DMD modes, the kth spatial DMD mode (shape of the mode) and the magnitude of the kth DMD mode, respectively. The term $\exp(\omega t) = \lambda^{t/\Delta t}$, where λ is the eigenvalue of the modes, describes the growth/decay and oscillation of the mode.

In this study, our objective of using DMD is to extract the modes corresponding to the key frequencies identified in the earlier part of the paper and to examine the topology of the modal reconstructions based on these modes as a means for identifying potential generation mechanisms. Discrete Fourier transform (DFT) based techniques such as notch filtering could be used for the purpose of modal reconstruction, but these DFT techniques require the data series to cover an integer number of the corresponding periods, and suffer from spectral leakage (Sayadi *et al.* 2014). Proper orthogonal decomposition (POD) analysis is another decomposition approach that could be used, but POD modes may contain multiple frequencies and therefore are not suitable for our analysis.

The total sample for the DMD analysis extends over a period of $11\,230\,\theta_o/U_o$, which corresponds roughly to 11.2 periods of the observed low frequency. Snapshots are extracted at every 400 time steps; this corresponds to a sampling frequency of $0.0642U_o/\theta_o$ and results in the extraction of a total of 721 snapshots. Each sample consists of the three velocity components u, v and w. In order to capture the key regions of the separated and reattaching flow, the spatial region over which the data are extracted covers $0 \leqslant x/\theta_o \leqslant 700$ and $0 \leqslant y/\theta_o \leqslant 100$.

In order to reduce the overall size of the dataset used in the DMD analysis to manageable levels, we employ a spatial subsampling where we first filter the velocity components by a box filter with width of $3\theta_o$, and then extract every eighth grid point in the x and z directions and every other point in y. This procedure leads to a total of 2.35 million samples per snapshot per observable, which is approximately 0.8 % of the total mesh nodes in the sample region. Finally, to avoid overfitting the complex dynamics of the fully turbulent field, instead of using the velocity data directly, we

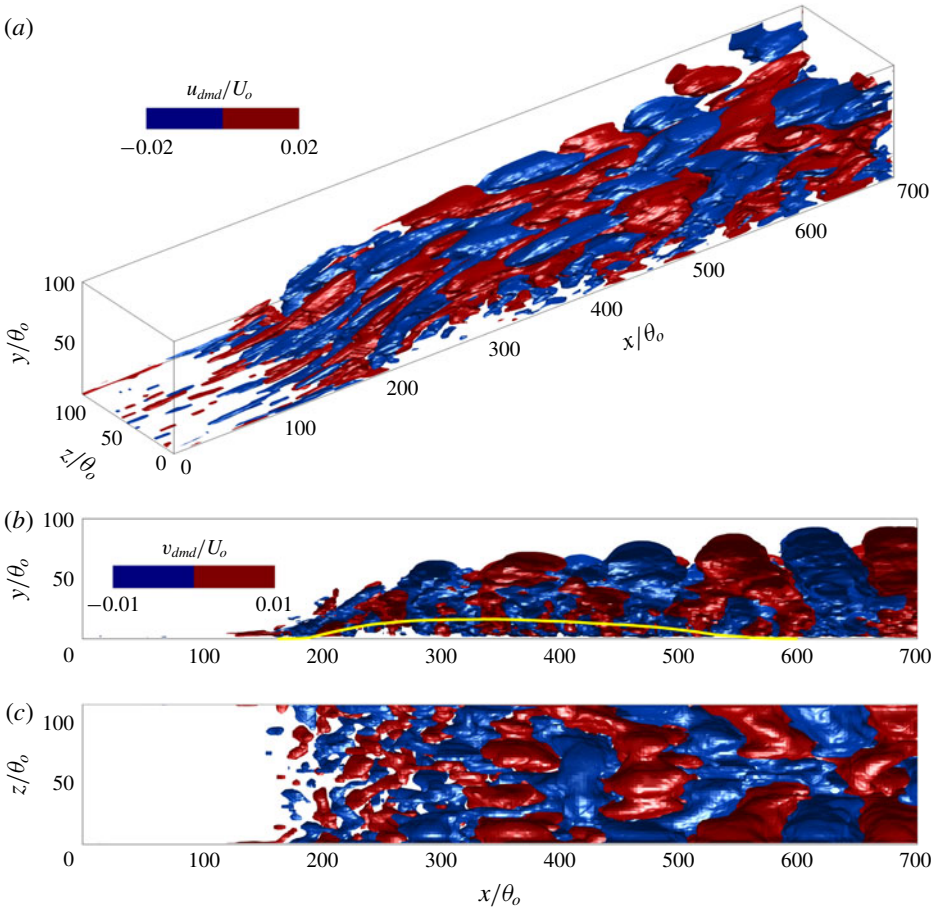

FIGURE 20. Isosurfaces of the real part of the high-frequency DMD mode $f_h\theta_o/U_o = 2.49 \times 10^{-3}$, $St_{L_{sep}} = 1.125$: (*a*) $u_{dmd}/U_o = \pm 0.02$; (*b*,*c*) $v_{dmd}/U_o = \pm 0.01$, top and side views, respectively. The solid line in (*b*) is for $U = 0$.

employ a 361-mode POD projection (one real mean mode and 180 complex-conjugate complex pairs), which serves as a spatio-temporal filter. This projection retains 98 % of the total kinetic energy, and 94 % of the turbulent kinetic energy of the flow.

The eigenvalues and (discrete) spectrum of the DMD modes are shown in figure 19. Since the flow is in a statistically saturated state, the eigenvalues lie mostly on or slightly inside the unit circle on the complex plane. Furthermore, due to the broadband nature of the flow, the spectrum exhibits a relatively continuous distribution of modes without any distinct and isolated peaks. This indicates that a significant number of modes are required to accurately reconstruct the dynamics of this flow. In the following, we focus on three modes whose frequencies are closest to those identified as the high ($f\theta_o/U_o = 0.0025$), medium ($f\theta_o/U_o = 0.002$) and low ($f\theta_o/U_o = 0.001$) frequencies in the previous sections, i.e. $f_h\theta_o/U_o = 2.49 \times 10^{-3}$, $f_m\theta_o/U_o = 1.97 \times 10^{-3}$ and $f_l\theta_o/U_o = 1.03 \times 10^{-4}$.

Figures 20 and 21 show DMD modes corresponding to the high- and mid-frequency spectral peaks. The key characteristic of these two modes that is visible from these plots is the highly regular arrangement of alternating structures separated in the

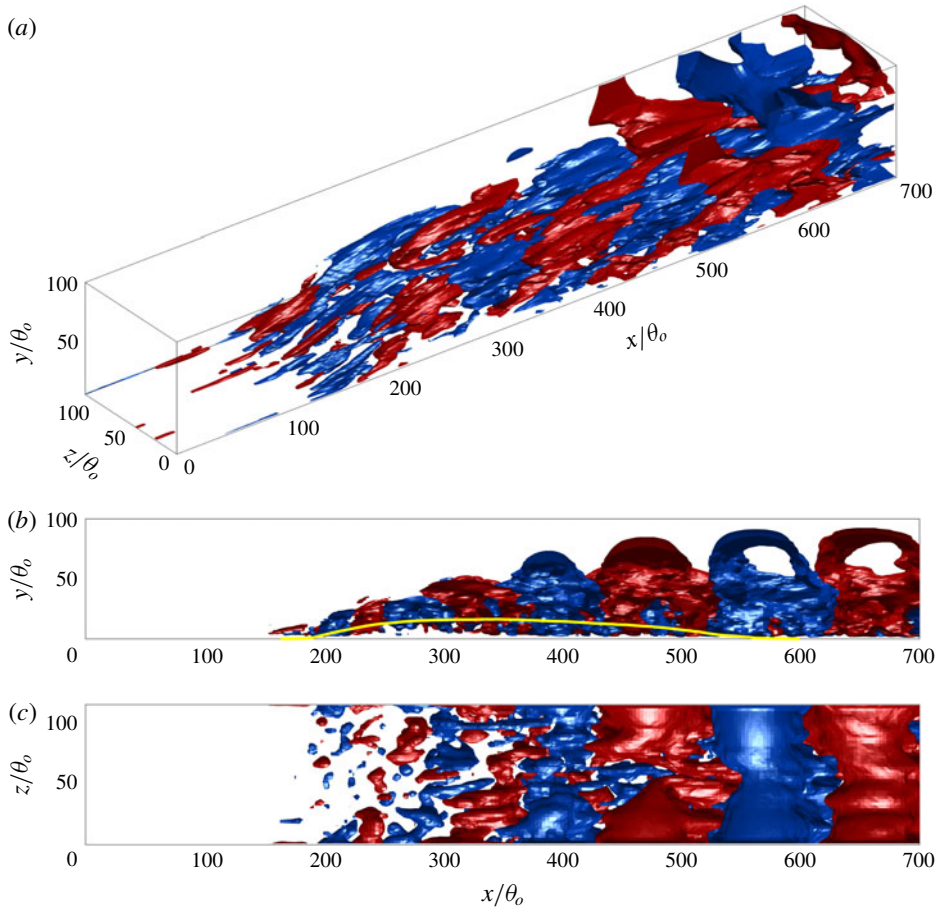

FIGURE 21. Isosurfaces of the real part of the mid-frequency DMD mode $f_m\theta_o/U_o = 1.97 \times 10^{-3}$, $St_{L_{sep}} = 0.90$. Colour/line style refers to figure 20.

streamwise direction. These structures also exhibit a considerable degree of coherence in the spanwise direction (figures 20*c* and 21*c*). The high-frequency mode appears similar to the λ-vortex structure formed by the oblique modes in a transitional boundary layer (Schmid & Henningson 2012). Both these features correspond well to the notion that these two modes are associated with the KH instability, and the modal structure corresponds primarily with spanwise vortex rollers.

The topology of the low-frequency mode (shown in figure 22) is quite different from that of the high-frequency modes discussed above and appears to be dominated by highly elongated streamwise structures. For example, the structure located near $z = 0$ starts from $x/\theta_o = 40$ and extends to $x/\theta_o = 410$; another one generated around $[x, z]/\theta_o = [100, 86]$ extends to $x/\theta_o = 270$ (figure 22*a*). Note that the simulation is periodic in the spanwise direction so that the structure at $z = L_z$ connects with the one at $z = 0$. Further downstream in the region where the free-stream APG vanishes, the streamwise structures connect and form larger structures. However, their two-dimensionality along the streamwise direction seems to be preserved. When compared with the high-frequency modes, the low-frequency mode has a much larger

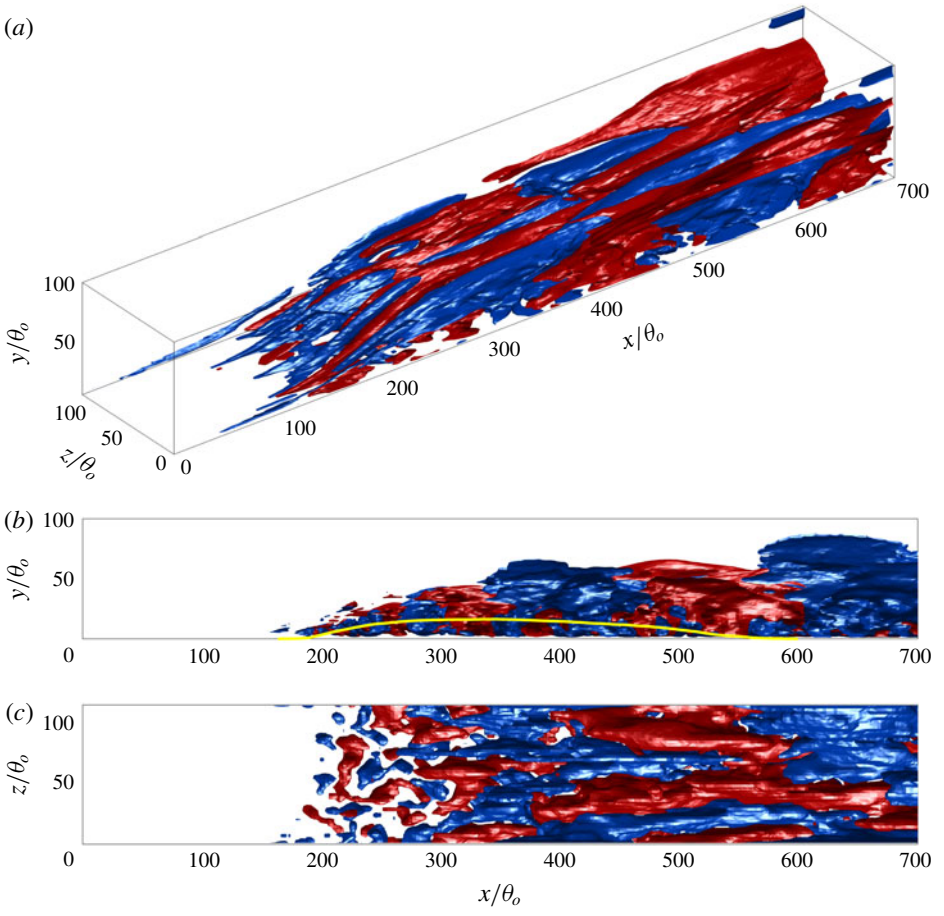

FIGURE 22. Isosurfaces of the real part of the low-frequency DMD mode $f_l\theta_o/U_o = 1.03 \times 10^{-3}$, $St_{L_{sep}} = 0.45$. Colour/line style refers to figure 20.

wavelength in the streamwise direction (figure 22*a*). The size of the structures grows abruptly near $x/\theta_o = 400$ (figure 22*b*,*c*).

The side view of this mode shows that there is also a significant spanwise-oriented signature in this mode. Furthermore, even structures that show a streamwise-oriented topology can 'shed' in a spanwise homogeneous manner, resulting in a noticeable spanwise-averaged signal, and that is likely what is happening in this flow: figure 23 shows the streamwise velocity component for the low-frequency DMD mode at four equally spaced phases in one cycle. The shedding of structures can be observed in the *x*–*y* slice contour, while the streamwise coherence persists in the *x*–*z* slices.

3.4. *Görtler instability as a mechanism for the low-frequency mode*

The topology of the low-frequency mode suggests that it could be related to Görtler vortices, which appear as streamwise-elongated structures in the boundary layers over concave walls. These Görtler vortices are generated by a centrifugal instability that destabilizes the flow when the direction of the wall-normal velocity gradient is opposite to the centrifugal force associated with the curvature of the streamlines

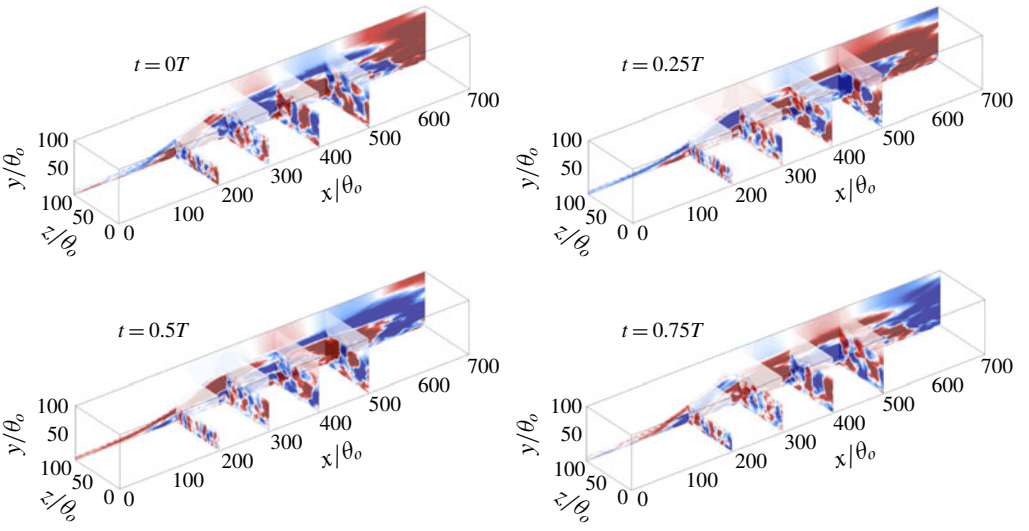

FIGURE 23. Contour of the streamwise velocity of the low-frequency DMD mode (refer to figure 22) at four equally spaced phases in one cycle (i.e. period of T).

(Görtler 1954), and previous studies on separated flows have suggested the presence of Görtler-type vortices (Settles, Fitzpatrick & Bogdonoff 1979; Loginov, Adams & Zheltovodov 2006; Priebe *et al.* 2016). Numerous previous studies on Görtler vortices have proposed a variety of threshold criteria for Görtler instability as well as the characteristic wavelength of the generated structures. In general, it is widely accepted that Görtler instability appears when the Görtler number, defined as

$$G_T = \frac{U_e\theta}{\nu}\sqrt{\frac{\theta}{R}}, \tag{3.6}$$

where U_e, θ and R are the free-stream velocity at the edge of the boundary layer, the local momentum thickness and the radius of curvature of the mean flow, respectively, exceeds 0.3 (Görtler 1954; Smith 1955). The most amplified wavelength in the spanwise direction is found to be λ_T, corresponding to $U_e\lambda_T/\nu\sqrt{\lambda_T/R} \approx 220$–$270$ (Smith 1955; Floryan & Saric 1982; Luchini & Bottaro 1998) or $\lambda_T \approx \delta - 2\delta$ (Smits & Dussauge 2006). However, the above scaling laws are for laminar flows and their applicability to turbulent flows is unclear. Tani (1962) proposed that the criterion for the onset of the Görtler instability is valid for turbulent flows provided the molecular viscosity is replaced by the eddy viscosity. It has also been suggested that $\delta/R \geqslant 0.01$ is the applicable criterion instigating Görtler instability for the case of TBLs (Hoffmann, Muck & Bradshaw 1985; Floryan 1991).

To examine these proposed criteria for the present flow, we calculate the effective turbulent eddy viscosity as (Spalart & Strelets 2000)

$$\nu_{t,eff} = -\frac{\overline{u_i'u_j'}S_{ij}}{2S_{ij}S_{ij}}, \tag{3.7}$$

and use $\nu_{tot} = \nu + \nu_{t,eff}$ to estimate the Görtler number. The analysis is applied in the region of mean streamline concavity shown in figure 24. It can be seen that,

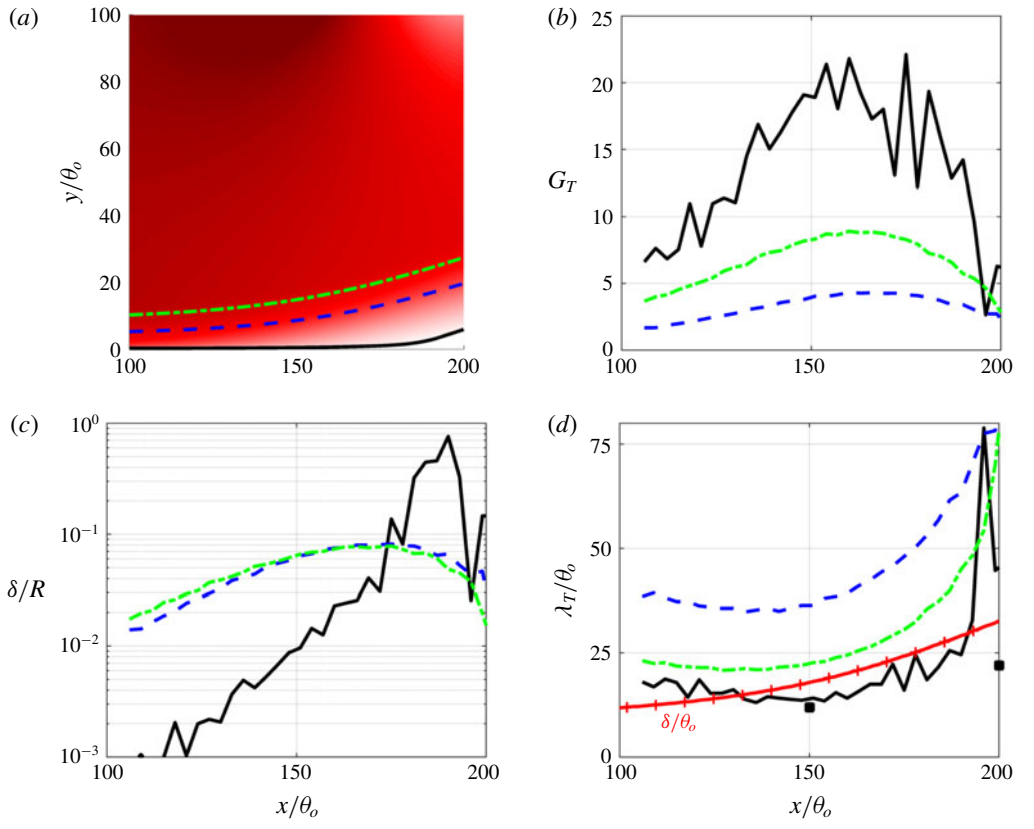

FIGURE 24. (*a*) Selected streamlines (solid, dashed and dash-dotted, respectively) for Görtler instability analysis; (*b*) Görtler number; (*c*) δ/R; and (*d*) most amplified spanwise wavelength predicted by $U_e\lambda_T/\nu_{tot}\sqrt{\lambda_T/R} = 250$. The red solid line with crosses is δ/θ_o for reference. Black markers are the length scale in the separated shear layer measured by the streamwise fluctuating velocity (figure 26).

when the boundary layer separates from the wall, the Görtler number ranges from approximately 5 to 21 in the near-wall region and δ/R ranges from 0.08 to 0.5. These values are well above the threshold proposed in previous studies, indicating the viability of the occurrence of Görtler instability. The most amplified spanwise wavelength (see figure 24*d*) is predicted to range from approximately $25\theta_o$ to $50\theta_o$ at $x = 180\theta_o$, which is in the range of (1–2)δ. The low-frequency DMD mode exhibits approximately four pairs of counter-rotating streamwise vortices in the spanwise direction near $x = 200\theta_o$ (figure 22*a*). This corresponds to a wavelength of 0.9δ, consistent with the predicted range of the most amplified wavelength of possible Görtler instability modes.

It is noted that, downstream of $x = 200\theta_o$, the mean streamlines become convex in shape but the sign of the velocity gradient remains unchanged except for the very near-wall region inside the separation bubble. Thus, while the conditions required for the Görtler instability no longer exist in this region, Görtler vortices that were generated upstream of the region continue to develop and grow on this region. As observed from the structures of the low-frequency DMD modes, the scale of the elongated streamwise

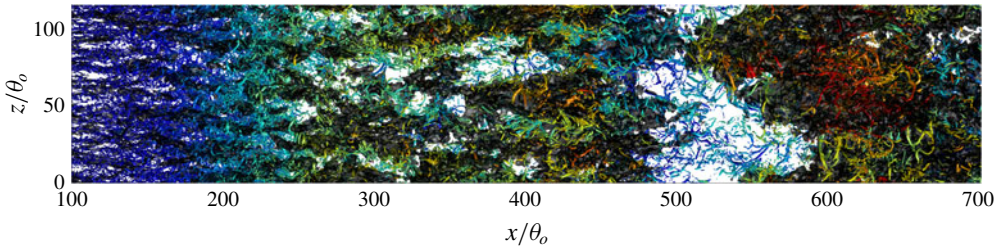

FIGURE 25. Top view of the instantaneous vortical structures shown by the isosurfaces of the secondary invariant of the velocity-gradient tensor Q, coloured by the distance from the wall. The dark-grey isosurfaces are $u' = -0.1U_o$. For an isometric view and colour map, refer to figure 5(*b*).

structures grows in the streamwise direction and the structures break down around $x = 400\theta_o$.

3.5. *Breakdown of Görtler vortices and turbulence structures*

In this section we examine the elongated streamwise structures in the TSB and their possible relationship to structures in the incoming TBL upstream of the separation bubble. The prominence of large-scale streamwise structures in ZPG TBLs at high Reynolds numbers is well known (Adrian, Meinhart & Tomkins 2000; Ganapathisubramani, Longmire & Marusic 2003; Hutchins & Marusic 2007), and these structures are amplified in the presence of an APG (Skote, Hanningson & Henkes 1998; Lee & Sung 2009; Harun *et al.* 2013). In studies on flow separation that employ suction and blowing (Abe *et al.* 2012; Abe 2017), large-scale structures identified by the streamwise velocity fluctuations were also observed but were attributed to the lifted and energized outer layer structures after flow separation. Our results of the DMD analysis, on the other hand, indicate that the streamwise-elongated structures are mostly amplified when the flow separates and streamline curvature becomes significant. This, however, does not necessarily imply that there is no link between the low-speed regions ('streaks') in the incoming boundary layer and the large-scale streamwise-oriented structures we have identified as Görtler vortices. The low-speed regions could serve as the perturbations for the initial development of the Görtler vortices. Similar to Priebe *et al.* (2016), we identified a time-delayed correlation between the appearance of a low-speed region in the incoming boundary layer and the occurrence of the Görtler vortices (not shown). This could be the reason why the occurrence of the elongated structures in the spanwise direction is highly unsteady, instead of being at fixed locations when the Görtler instability is triggered by prescribed upstream disturbances (see Floryan & Saric 1982; among others).

Figure 25 shows the top view of the turbulent structures exhibited in figure 5. The streamwise alignment of the structures ($x < 450\theta_o$) is quite evident and the scale of the low-speed region increases as the flow travels downstream (e.g. the dark grey isosurface of $u' = -0.1U_o$ at $x/\theta_o = 300$ is much thicker than the ones at $x/\theta_o = 100$ and 200, which appear to be thin rod-like regions). The growth of Görtler vortices in a laminar flow over a concave wall has been examined in previous studies (Bippes & Görtler 1972; Swearingen & Blackwelder 1983; Smith & Walker 1989; Li & Malik 1995) and one observation is that the continuous ejection of fluid from the low-speed region by the counter-rotating vortices creates a marked retardation of flow in the

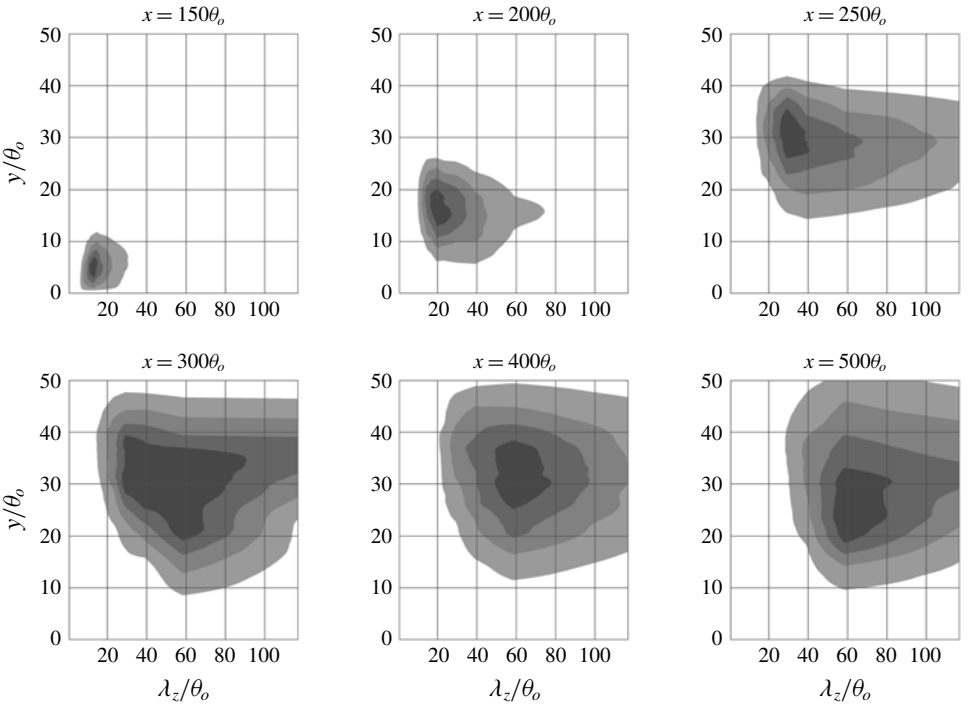

FIGURE 26. Pre-multiplied spanwise energy spectrum of the streamwise fluctuating velocity, examined at several streamwise locations. Each map is normalized by its maximum, and contours are shown at level 0.8, 0.6, 0.4 and 0.2, from dark to light, respectively.

upwash region and an APG in the streamwise direction, which has the dual effect of both forcing the vortices away from the wall and also increasing the spanwise distance between the vortices (Bippes & Görtler 1972; Smith & Walker 1989). The behaviour of the streamwise structures shown in our simulation is in line with this observation.

The scale of the streamwise structures in the spanwise direction is examined using the pre-multiplied energy spectrum of u', and figure 26 shows the spectrum at several streamwise locations. The growth of the spanwise length scale is clearly seen. The spanwise length scale of these structures is approximately $20\theta_o$ to $30\theta_o$ in the upstream side of the separation bubble, which agrees reasonably well with the most unstable wavelength predicted by the Görtler instability (refer to figure 24*d*). From $x = 300\theta_o$ the wavelength changes to 60θ, consistent with the observation of the low-frequency DMD mode, which shows that the structures merge after the crest of the separation bubble.

In previous studies, it has been proposed that Görtler vortices may break down due to four processes: (a) Tollmien–Schlichting waves. (b) Nonlinear development of Görtler vortices and energy cascades down from the fundamental into the higher harmonics and the mean flow. (c) Secondary instabilities that generate a retarded region in the upstream flow region between Görtler vortices and the formation of transverse vortices (Bippes & Görtler 1972; Hall 1982; Smith & Walker 1989). Linear stability theory has revealed two types of secondary instabilities that help break down the Görtler vortices in laminar flows: a sinuous (odd) mode that perturbs the Görtler

vortices in a wavy manner, and a varicose (even) mode that breaks up Görtler vortices into a series of 'knotty' structures (see Swearingen & Blackwelder 1983; Li & Malik 1995; among others). None of these processes is clearly evident in the single DMD mode reconstruction, and the structures in the flow velocity seem to exhibit both streamwise waviness and breakup. Which mode (if any) dominates the breakup of vortices in this flow is unclear from the current simulations. (d) The vortex merging/pairing process. As discussed regarding the frequency change (figure 14) and the vortex development (figures 17 and 18), it is possible that the breakup of the Görtler vortices is associated with the merging/pairing of the spanwise roller vortices. The DMD mode at the low frequency does exhibit a spanwise staggered signature (figure 22*b*), which provides further support for this possibility. However, this correlation does not necessarily imply causation.

4. Conclusions

Direct numerical simulations of a turbulent boundary layer over a flat plate with induced separation are performed with the aim of investigating the spatio-temporal dynamics of turbulent separation bubbles (TSBs). The separation is induced by employing a transpiration boundary condition on the top boundary of the computational domain. Two different transpiration velocity profiles are employed: one with suction followed by blowing and the other with suction only. Compared with the TSB created by the suction–blowing profile, the suction-only case exhibits a pressure gradient and Reynolds stress distribution that are in much better qualitative agreement with separated flows over airfoils and in diffusers.

Focusing on the suction-only case, we show that the high- and mid-frequency motion is well characterized by flow physics that corresponds to that observed in a plane turbulent mixing layer. In particular, these modes are associated with the formation and shedding of spanwise-oriented rollers, as also confirmed by DMD analysis. The characteristic frequency of these modes does not scale with U/L_{sep} because in both the TSB-SB and TSB-SO cases this mode occurs at a similar frequency, while the length of the mean separation bubble differs by a factor of approximately 2.4.

The suction-only case exhibits a low-frequency unsteadiness (i.e. breathing/flapping) in the separation bubble at a frequency that is two-and-a-half times smaller than the dominant high frequency. A similar low-frequency motion is not observed in the suction–blowing case. The low-frequency motion observed here appears as a spatio-temporal variation of the separation region: the separation bubble opens at regular intervals corresponding to this low frequency and releases a large-scale conglomeration of vortices that convects downstream and is associated with low-speed and even reversed flow. DMD analysis of the flow, however, shows that the topological signature of this mode does not simply correspond to the merging of spanwise rollers. The single DMD mode at the low frequency exhibits a topology that is dominated by highly elongated streamwise structures that extend from nearly the point of separation to downstream of the mean reattachment point. Analysis of the data shows that the streamline curvature does exceed the threshold for Görtler instability and the properties of the elongated streamwise structures, such as spanwise wavelength, agree with the values reported in the literature. Their periodic breakdown, possibly a secondary instability, could cause the observed low-frequency mode or modulate the vortex merger. The absence of the low-frequency motion in the TSB-SB case may be due to the forced closure (reattachment) of the separation bubble, which does not allow natural instabilities, especially those with large time and length scales, to grow.

The simulations, however, do not indicate the mechanism for the breakdown of the elongated streamwise structures and the subsequent formation of the large-scale eddies that are released from the separation bubble. The scale separation between the low and high frequencies in the current study is limited due to the relatively low Reynolds numbers. The KH instability is inviscid in nature and the characteristic vortex shedding frequency scales with the outer scales. Therefore, the high- and medium-frequency motions are not expected to change much with the Reynolds number. In the simulation by Abe (2017), the peaks in the spectra of wall pressure do not change much between $Re_\theta = 300$ and 900 (refer to figure 21 in Abe (2017)), given the minor change in L_{sep}. Ongoing studies are focused on higher Reynolds numbers where a larger scale separation will enable a clearer distinction between the dominant spatio-temporal scales in the flow. Lastly, the effects of streamline curvature cannot be dismissed in the separation bubble but the curvature can be altered by changing the magnitude of the APG. A very mild APG may cause small streamline curvature and prevent the amplification of the Görtler vortices. Some of these issues are presently under study.

Acknowledgements

The authors would like to thank Dr L. Cattafesta (Florida State University), Dr C. Rowley (Princeton University) and Dr D. Gayme (Johns Hopkins University) for fruitful discussions. The authors also acknowledge the support from AFOSR grant FA9550-17-1-0084, monitored by Dr G. Abate. The simulations were performed at the Texas Advanced Computing Center (TACC) Stampede-2 cluster.

Appendix. Dynamic mode decomposition

The DMD analysis and field reconstruction are performed by the following procedure:

(*a*) Collect snapshots of data ($\boldsymbol{\phi} = [\boldsymbol{\phi}_1, \boldsymbol{\phi}_2, \ldots, \boldsymbol{\phi}_N]$, where each column of matrix $\boldsymbol{\phi}$ consists of a vector of observables (reshaped to one dimension if sampled in two or three dimensions) at t_i and N is the total number of snapshots) from the simulation at several time instants that are equally spaced in time. Vector $\boldsymbol{\phi}$ might correspond, for instance, to the velocity components or pressure for a set of grid points in a region of the flow. Each column vector $\boldsymbol{\phi}$ can include several observables. If the observables are sampled at M spatial locations and a total of P observables are used, the size of the matrix $\boldsymbol{\phi}$ is $[M \times P,\ N]$.

(*b*) Arrange the data $\boldsymbol{\phi}$ into matrices:

$$\boldsymbol{X} \equiv [\boldsymbol{\phi}_1, \boldsymbol{\phi}_2, \ldots, \boldsymbol{\phi}_{N-1}], \quad \boldsymbol{Y} \equiv [\boldsymbol{\phi}_2, \boldsymbol{\phi}_3, \ldots, \boldsymbol{\phi}_N]. \tag{A 1}$$

(*c*) Dimensionality reduction: compute the (reduced) singular value decomposition of $\boldsymbol{X}$, i.e.

$$\boldsymbol{X}' = \boldsymbol{U}\boldsymbol{\Sigma}\boldsymbol{V}^T, \tag{A 2}$$

where $\boldsymbol{U}$ is of size $[M \times P,\ r]$, $\boldsymbol{\Sigma}$ is $r \times r$ and $\boldsymbol{V}$ is $[N, r]$, where r is the reduced rank of $\boldsymbol{X}'$, or the total number of the conjugated modes.

(*d*) Define the matrix (size $[r, r]$)

$$\tilde{\boldsymbol{A}} \equiv \boldsymbol{U}^T\boldsymbol{Y}\boldsymbol{V}\boldsymbol{\Sigma}^{-1}. \tag{A 3}$$

(*e*) Compute eigenvalues (λ) and eigenvectors ($\boldsymbol{w}$) of $\tilde{\boldsymbol{A}}$, writing

$$\tilde{\boldsymbol{A}}\boldsymbol{w} = \lambda \boldsymbol{w}. \tag{A 4}$$

(*f*) The DMD mode corresponding to the DMD eigenvalue λ is then given by

$$\boldsymbol{\psi} \equiv \boldsymbol{Y}\boldsymbol{V}\boldsymbol{\Sigma}^{-1}\boldsymbol{w}. \tag{A 5}$$

In this study, the modes are normalized by their initial amplitudes in $\boldsymbol{\phi}_1$.

(*g*) Calculate the (initial) amplitude of each mode, i.e. the contribution of each mode to the first snapshot:

$$\boldsymbol{b} = \boldsymbol{\psi}^{-1}\boldsymbol{\phi}_1. \tag{A 6}$$

(*h*) Obtain the frequency of each mode,

$$f = \mathrm{Im}(\ln \lambda)/(2\pi \Delta t) \tag{A 7}$$

or $f = \tan^{-1}[\mathrm{Im}(\boldsymbol{\psi})/\mathrm{Re}(\boldsymbol{\psi})]/(2\pi\Delta t)$.

(*i*) Define $\omega = \ln(\lambda)/\Delta t$, and reconstruct the data series by

$$\boldsymbol{\phi}_{dmd}(t) \equiv \boldsymbol{\psi}\, \exp(\boldsymbol{\omega} t)\boldsymbol{b}, \tag{A 8}$$

where on the right-hand side $\boldsymbol{\psi}$ gives the shape of the mode, $\boldsymbol{b}$ determines the magnitude and the exponential term represents decay/growth.

REFERENCES

ABE, H. 2017 Reynolds-number dependence of wall-pressure fluctuations in a pressure-induced turbulent separation bubble. *J. Fluid Mech.* **833**, 563–598.

ABE, H. 2019 Direct numerical simulation of a turbulent boundary layer with separation and reattachment over a range of Reynolds numbers. *Fluid Dyn. Res.* **51**, 011409.

ABE, H., MIZOBUCHI, Y., MATSUO, Y. & SPALART, P. R. 2012 DNS and modeling of a turbulent boundary layer with separation and reattachment over a range of Reynolds numbers. In *CTR Annual Research Briefs*, pp. 311–322. Center for Turbulence Research.

ADRIAN, R. J., MEINHART, C. D. & TOMKINS, C. D. 2000 Vortex organization in the outer region of the turbulent boundary layer. *J. Fluid Mech.* **422**, 1–54.

ALAM, M. & SANDHAM, N. D. 2000 Direct numerical simulation of 'short' laminar separation bubbles with turbulent reattachment. *J. Fluid Mech.* **410**, 1–28.

ALVING, A. E. & FERNHOLZ, H. H. 1996 Turbulence measurements around a mild separation bubble and downstream of reattachment. *J. Fluid Mech.* **322**, 297–328.

ASADA, K. & KAWAI, S. 2018 Large-eddy simulation of airfoil flow near stall condition at Reynolds number 2.1×10^6. *Phys. Fluid.* **30**, 085103.

BALAKUMAR, P. 2017 Direct numerical simulation of flows over an NACA-0012 airfoil at low and moderate Reynolds numbers. In *2017 Fluid Dynamics Conference, AIAA AVIATION Forum,* pp. AIAA 2017–3978. AIAA AVIATION Forum.

BIPPES, H. & GÖRTLER, H. 1972 Dreidimensionale stoerungen in der grenzschicht an einer konkaven wand. *Acta Mech.* **14**, 251–267.

BROWN, B. L. & ROSHKO, A. 1974 On density effects and large structure in turbulent mixing layers. *J. Fluid Mech.* **64**, 775–816.

CHEN, K. K., TU, J. H. & ROWLEY, C. W. 2012 Variants of dynamic mode decomposition: boundary condition, Koopman, and Fourier analyses. *J. Nonlinear Sci.* **22**, 887–915.

CHERRY, N. J., HILLIER, R. & LATOUR, M. E. M. P. 1984 Unsteady measurements in a separated and reattaching flow. *J. Fluid Mech.* **144**, 13–46.

CLEMENS, N. T. & NARAYANASWAMY, V. 2014 Low-frequency unsteadiness of shock wave/turbulent boundary layer interactions. *Annu. Rev. Fluid Mech.* **46**, 469–492.

COLEMAN, G. N., RUMSEY, C. L. & SPALART, P. R. 2018 Numerical study of turbulent separation bubbles with varying pressure gradient and Reynolds number. *J. Fluid Mech.* **847**, 28–70.

DANDOIS, J., GARNIER, E. & SAGAUT, P. 2007 Numerical simulation of active separation control by a synthetic jet. *J. Fluid Mech.* **574**, 25–58.

DIANAT, M. & CASTRO, I. P. 1991 Turbulence in a separated boundary layer. *J. Fluid Mech.* **226**, 91–123.

DON, W. S. & GOTTLIEB, D. 1990 Spectral simulation of unsteady compressible flow past a circular cylinder. In *NASA Contractor Report 182030*; ICASE Report 90-29.

DRIVER, D. M., SEEGMILLER, H. L. & MARVIN, J. G. 1987 Time-dependent behavior of a reattaching shear layer. *AIAA J.* **25** (7), 914–919.

DURST, F. & TROPEA, C. 1982 Flows over two-dimensional backward-facing steps. In *Proc. IUTAM Symp.*, pp. 41–52. Springer International Publishing AG.

DUSSAUGE, J.-P., DUPONT, P. & DEBIÈVE, J.-F. 2006 Unsteadiness in shock wave boundary layer interactions with separation. *Aerosp. Sci. Technol.* **10**, 85–91.

EATON, J. K. & JOHNSTON, J. P. 1982 Low-frequency unsteadiness of a reattaching turbulent boundary layer. In *Proc. 3rd Intl. Symp. Turbul. Shear Flow*, pp. 162–170. Springer.

FLORYAN, J. M. 1991 On the görtler instability of boundary layers. *Prog. Aerosp. Sci.* **28**, 235–271.

FLORYAN, J. M. & SARIC, W. 1982 Stability of görtler vortices in boundary layers. *AIAA J.* **20**, 316–324.

GANAPATHISUBRAMANI, B., LONGMIRE, E. K. & MARUSIC, I. 2003 Characteristics of vortex packets in turbulent boundary layers. *J. Fluid Mech.* **478**, 35–46.

GASTER, M. 1963 On stability of parallel flows and the behaviour of separation bubbles. PhD thesis, University of London.

GERICH, D. & ECKELMANN, H. 1982 Influence of end plates and free ends on the shedding frequency of circular cylinders. *J. Fluid Mech.* **122**, 109–121.

GÖRTLER, H. 1954 On the three-dimensional instability of laminar boundary layer on concave walls. In *National Advisory Committee for Aeronautics, Technical Memorandum 1375*; Translation of 'Über eine dreidimensionale Instabilität laminarer Grenzschichten an konkaven Wänden'.' Ges. d. Wiss. Göttingen, Nachr. a. d. Math., Bd. 2, Nr. 1, 1940.

HAIN, R., KÄHLER, C. J. & RADESPIEL, R. 2009 Dynamics of laminar separation bubbles at low-Reynolds-number aerofoils. *J. Fluid Mech.* **630**, 129–153.

HALL, P. 1982 On the nonlinear evolution of görtler vortices in non-parallel boundary layers. *IMA J. Appl. Maths* **29**, 173–196.

HALL, S. D., BEHNIA, C. A. J. F. M. & MORRISON, G. L. 2003 Investigation of the secondary corner vortices in a benchmark turbulent backward-facing step using cross-correlation particle imaging velocimetry. *Exp. Fluids* **35**, 139–151.

HAMMOND, D. A. & REDEKOPP, L. G. 1998 Local and global instability properties of separation bubbles. *Eur. J. Mech. (*B*/Fluids)* **17**, 145–164.

HARUN, Z., MONTY, J. P., MATHIS, R. & MARUSIC, I. 2013 Pressure gradient effects on the large-scale structure of turbulent boundary layers. *J. Fluid Mech.* **715**, 477–498.

HASAN, M. A. Z. 1992 The flow over a backward-facing step under controlled perturbation: laminar separation. *J. Fluid Mech.* **238**, 73–96.

HEENAN, F. & MORRISON, J. F. 1998 Passive control of pressure fluctuations generated by separated flow. *AIAA J.* **36** (6), 1014–1022.

HOFFMANN, P. H., MUCK, K. C. & BRADSHAW, P. 1985 The effects of concave surface curvature on turbulent boundary layers. *J. Fluid Mech.* **164**, 371–403.

HORTON, H. P. 1968 Laminar separation in two and three-dimensional incompressible flow. PhD thesis, University of London.

HUDY, L. M. & NAGUIB, A. 2007 Stochastic estimation of a separated-flow field using wall-pressure-array measurements. *Phys. Fluids* **19**, 024103.

HUERRE, P. & MONKEWITZ, P. A. 1985 Absolute and convective instabilities in free shear layers. *J. Fluid Mech.* **159**, 151–168.

HUTCHINS, N. & MARUSIC, I. 2007 Evidence of very long meandering features in the logarithmic region of turbulent boundary layers. *J. Fluid Mech.* **579**, 1–28.

JONES, L. E., SANDBERG, R. D. & SANDHAM, N. D. 2008 Direct numerical simulations of forced and unforced separation bubbles on an airfoil at incidence. *J. Fluid Mech.* **602**, 175–207.

JONES, L. E., SANDBERG, R. D. & SANDHAM, N. D. 2010 Stability and receptivity characteristics of a laminar separation bubble on an aerofoil. *J. Fluid Mech.* **648**, 257–296.

JONES, M. 1934 Stalling. *J. R. Aero. Soc.* **38** (285), 753–770.

KALTENBACH, H. J., FATICA, M., MITTAL, R., LUND, T. S. & MOIN, P. 1999 Study of flow in a planar asymmetric diffuser using large-eddy simulation. *J. Fluid Mech.* **390**, 151–185.

KIM, D.-H., YANG, J.-H., CHANG, J.-W. & CHUNG, J. 2009 Boundary layer and near-wake measurements of NACA 0012 airfoil at low Reynolds numbers. In *47th AIAA Aerospace Sciences Meeting,* pp. AIAA 2009–1472. AIAA AVIATION Forum.

KIYA, M. & SASAKI, K. 1985 Structure of large-scale vortices and unsteady reverse flow in the reattaching zone of a turbulent separation bubble. *J. Fluid Mech.* **154**, 463–491.

KOTAPATI, R., MITTAL, R., MARXEN, O., HAM, F., YOU, D. & LOUIS, N. C. 2010 Nonlinear dynamics and synthetic-jet-based control of a canonical separated flow. *J. Fluid Mech.* **654**, 65–97.

LEE, J.-H. & SUNG, H. J. 2009 Structures in turbulent boundary layers subjected to adverse pressure gradients. *J. Fluid Mech.* **639**, 101–131.

LI, F. & MALIK, M. R. 1995 Fundamental and subharmonic secondary instabilities of görtler vortices. *J. Fluid Mech.* **297**, 77–100.

LIEPMANN, H. W. & LAUFER, J. 1947 Investigation of free turbulent mixing. In *NACA Tech. Note, no.* 1257.

LOGINOV, M. S., ADAMS, N. A. & ZHELTOVODOV, A. A. 2006 Large-eddy simulation of shock-wave/turbulent-boundary-layer interaction. *J. Fluid Mech.* **565**, 135–169.

LUCHINI, P. & BOTTARO, A. 1998 Görtler vortices: a backward-in-time approach to the receptivity problem. *J. Fluid Mech.* **363**, 1–23.

LUND, T., WU, X. & SQUIRES, K. 1998 Generation of turbulent inflow data for spatially- developing boundary layer simulations. *J. Comput. Phys.* **140**, 233–258.

MARQUILLIE, M. & EHRENSTEIN, U. 2003 On the onset of nonlinear oscillations in a separating boundary-layer flow. *J. Fluid Mech.* **490**, 168–188.

MARXEN, O. & HENNINGSON, D. S. 2010 The effect of small-amplitude convective disturbances on the size and bursting of a laminar separation bubble. *J. Fluid Mech.* **671**, 1–33.

MARXEN, O. & RIST, U. 2010 Mean flow deformation in a laminar separation bubble: separation and stability characteristics. *J. Fluid Mech.* **660**, 37–54.

MARXEN, O., RIST, U. & SAGNER, W. 2003 A combined experimental/numerical study of unsteady phenomena in a laminar separation bubble. *Flow Turbul. Comb.* **71**, 133–146.

MCGUINEESS, M. 1978 Flow with a separation bubble – steady and unsteady aspects. PhD thesis, Cambridge University.

MICHELIS, T., YARUSEVYCH, S. & KOTSNOIS, M. 2018 On the origin of spanwise vortex deformations in laminar separation bubbles. *J. Fluid Mech.* **841**, 81–108.

MITTAL, R., DONG, H., BOZKURTTAS, M., NAJJAR, F., VARGAS, A. & VON LOEBBECKE, A. 2008 A versatile sharp interface immersed boundary method for incompressible flows with complex boundaries. *J. Comput. Phys.* **227**, 4825–4852.

MOHAMMED-TAIFOUR, A. & WEISS, J. 2016 Unsteadiness in a large turbulent separation bubble. *J. Fluid Mech.* **799**, 383–412.

MORGAN, B., LARSSON, J., KAWAI, S. & LELE, S. K. 2011 Improving low-frequency characteristics of recycling/rescaling inflow turbulence generation. *AIAA J.* **49**, 582–597.

NA, Y. & MOIN, P. 1998*a* Direct numerical simulation of a separated turbulent boundary layer. *J. Fluid Mech.* **374**, 379–405.

NA, Y. & MOIN, P. 1998*b* The structure of wall-pressure fluctuations in turbulent boundary layers with adverse pressure gradient and separation. *J. Fluid Mech.* **377**, 347–373.

NADGE, P. M. & GOVARDHAN, R. N. 2014 High Reynolds number flow over a backward-facing step: structure of the mean separation bubble. *Exp. Fluids* **55**, 1657.

NAJJAR, F. M. & BALACHANDAR, S. 1998 Low-frequency unsteadiness in the wake of a normal flat plate. *J. Fluid Mech.* **370**, 101–147.

OWEN, P. R. & KLANFER, L. 1953 On the laminar boundary layer separation from the leading edge of a thin aerofoil. In *ARC Conf. Proc.*, p. CP 220.

PANTANO, C. & SARKAR, S. 2002 A study of compressibility effects in the high-speed turbulent shear layer using direct simulation. *J. Fluid Mech.* **451**, 329–371.

PATRICK, W. P. 1987 Flowfield measurements in a separated and reattached flat plate turbulent boundary layer. In *NASA Tech. Rep.*, p. 4052.

PAULEY, L. L., MOIN, P. & REYNOLDS, W. C. 1990 The structure of two-dimensional separation. *J. Fluid Mech.* **220**, 397–411.

PERRY, A. E. & FAIRLIE, B. D. 1975 A study of turbulent boundary-layer separation and reattachment. *J. Fluid Mech.* **69**, 657–672.

POPE, S. B. 2000 *Turbulent Flows*. Cambridge University Press.

PRIEBE, S., TU, J. H., ROWLEY, C. W. & MARTÍN, M. P. 2016 Low-frequency dynamics in a shock-induced separated flow. *J. Fluid Mech.* **807**, 441–477.

RINOIE, K. & TAKEMURA, N. 2004 Oscillating behaviour of laminar separation bubble formed on an aerofoil near stall. *Aeronaut. J.* **108**, 153–163.

RIST, U. & MAUCHER, U. 2002 Investigations of time-growing instabilities in laminar separation bubbles. *Eur. J. Mech. (*B*/Fluids)* **21**, 495–509.

SAYADI, T., SCHMID, P. J., NICHOLS, J. W. & MOIN, P. 2014 Reduced-order representation of near-wall structures in the late transitional boundary layer. *J. Fluid Mech.* **748**, 278–301.

SCHLATTER, P. & ÖRLÜ, R. 2010 Assessment of direct numerical simulation data of turbulent boundary layers. *J. Fluid Mech.* **659**, 116–126.

SCHMID, P. J. 2010 Dynamic mode decomposition of numerical and experimental data. *J. Fluid Mech.* **656**, 5–28.

SCHMID, P. J. & HENNINGSON, D. S. 2012 *Stability and Transition in Shear Flows*, vol. 142. Springer Science & Business Media.

SEO, J. H., CADIEUX, F., MITTAL, R., DEEM, E. & LOUIS, N. C. 2018 Effect of synthetic jet modulation schemes on the reduction of a laminar separation bubble. *Phys. Rev. Fluids* **3**, 033901.

SETTLES, G. S., FITZPATRICK, T. J. & BOGDONOFF, S. M. 1979 Detailed study of attached and separated compression corner flowfields in high Reynolds number supersonic flow. *AIAA J.* **16**, 579–585.

SKOTE, M. & HANNINGSON, D. 2002 Direct numerical simulation of a separated turbulent boundary layer. *J. Fluid Mech.* **471**, 107–136.

SKOTE, M., HANNINGSON, D. & HENKES, R. 1998 Direct numerical simulation of self-similar turbulent boundary layers in adverse pressure gradients. *Flow Turbul. Combust.* **60**, 47–85.

SMITH, A. M. O. 1955 On the growth of Taylor–Görtler vortices along highly concave wall. *Q. Appl. Mech.* **13**, 233–262.

SMITH, C. R. & WALKER, J. D. A. 1989 *Three Dimensional Vortex Interactions in Turbulent Boundary Layers*, pp. 1–96. Lehigh University, Department of Mechanical Engineering and Mechanics.

SMITS, A. J. & DUSSAUGE, J.-P. 2006 *Turbulent Shear Layers in Supersonic Flow*, 2nd edn. Springer.

SONG, S., DEGRAAFF, D. B. & EATON, J. K. 2000 Experimental study of a separating, reattaching, and redeveloping flow over a smoothly contoured ramp. *Intl J. Heat Fluid Flow* **21**, 512–519.

SPALART, P. R. & COLEMAN, G. N. 1997 Numerical study of a separation bubble with heat transfer. *Eur. J. Mech. (*B*/Fluids)* **16**, 169–189.

SPALART, P. R., STRELETS, M. & TRAVIN, A. 2006 Direct numerical simulation of large-eddy-break-up devices in a boundary layer. *Intl J. Heat Fluid Flow* **27**, 902–910.

SPALART, P. R. & STRELETS, M. KH. 2000 Mechanisms of transition and heat transfer in a separation bubble. *J. Fluid Mech.* **403**, 329–349.

SPAZZINI, P. G., LUSO, G., ONORATO, M., ZURLO, N. & CICCA, G. M. D. 2001 Unsteady behavior of back-facing step flow. *Exp. Fluids* **30**, 551–561.

STRYKOWSKI, P. J. & NICCUM, D. L. 1991 The stability of countercurrent mixing layers in circular jets. *J. Fluid Mech.* **227**, 309–343.

SWEARINGEN, J. D. & BLACKWELDER, R. F. 1983 Parameters controlling the spacing of streamwise vortices on a concave wall. *AIAA J.* **83**, 0380.

TAFTI, D. K. & VANKA, S. P. 1991 A three-dimensional numerical study of flow separation and reattachment on a blunt plate. *Phys. Fluids* **3**, 2887.

TANI, I. 1962 Production of longitudinal vortices in the boundary layer along a concave wall. *J. Geophys. Res.* **67**, 3075–3080.

TANI, T. 1964 Low-speed flows involving bubble separations. *Prog. Aerosp. Sci.* **5**, 70–103.

TENAUD, C., PODVIN, B., FRAIGNEAU, Y. & DARU, V. 2016 On wall pressure fluctuations and their coupling with vortex dynamics in a separated–reattached turbulent flow over a blunt flat plate. *Intl J. Heat Fluid Flow* **61**, 730–748.

TOUBER, E. & SANDHAM, N. D. 2009 Comparison of three large-eddy simulations of shock-induced turbulent separation bubbles. *Shock Waves* **19**, 469–478.

TROUTT, T. R., SCHEELKE, B. & NORMAN, T. R. 1984 Organized structures in a reattaching separated flow field. *J. Fluid Mech.* **143**, 413–427.

WEE, D., YI, T., ANNASWAMY, A. & GHONIEM, A. F. 2004 Self-sustained oscillations and vortex shedding in backward-facing step flows: simulation and linear instability analysis. *Phys. Fluids* **16**, 3361.

WEISS, J., MOHAMMED-TAIFOUR, A. & SCHWAAB, Q. 2015 Unsteady behavior of a pressure-induced turbulent separation bubble. *AIAA J.* **53**, 2634–2645.

WU, S. J., MIAU, J. J., HU, C. C. & CHOU, J. H. 2005 On low-frequency modulations and three-dimensionality in vortex shedding behind a normal plate. *J. Fluid Mech.* **526**, 117–146.

WU, W., MENEVEAU, C. & MITTAL, R. 2019 Dynamics of natural and perturbed turbulent separation bubbles. In *Eleventh International Symposium on Turbulence and Shear Flow Phenomena (TSFP11), Southampton, UK, 30 July–2 August, 2019*.

WU, W. & PIOMELLI, U. 2018 Effects of surface roughness on a separating turbulent boundary layer. *J. Fluid Mech.* **841**, 552–580.

WU, W., SEO, J.-H., MENEVEAU, C. & MITTAL, R. 2018 Response of a laminar separation bubble to forcing with zero-net mass flux jets. In *Proc. 2018 Flow Control Conference, AIAA AVIATION Forum, (AIAA 2018-4018)*.

WU, X., MOIN, P., WALLACE, J. M., SKARDA, J., LOZANO-DURAN, A. & HICKEY, J.-P. 2017 Transitional-turbulent spots and turbulent-turbulent spots in boundary layers. In *Proceedings of National Academy of Sciences, USA*, p. 1704671114. PNAS.